THE ASTROPHYSICAL JOURNAL, 436:467–490, 1994 December 1

COLD DARK MATTER. I. THE FORMATION OF DARK HALOS

JAMES M. GELB[1] AND EDMUND BERTSCHINGER
Department of Physics, Massachusetts Institute of Technology, Cambridge, MA 02139
Received 1992 December 22; accepted 1994 May 31

ABSTRACT

We use numerical simulations of critically closed cold dark matter (CDM) models to study the effects of numerical resolution on observable quantities. We study simulations with up to 256^3 particles using the particle-mesh (PM) method and with up to 144^3 particles using the adaptive particle-particle–mesh (P^3M) method. Comparisons of galaxy halo distributions are made among the various simulations. We also compare distributions with observations, and we explore methods for identifying halos, including a new algorithm that finds all particles within closed contours of the smoothed density field surrounding a peak. The simulated halos show more substructure than predicted by the Press-Schechter theory. We are able to rule out all $\Omega = 1$ CDM models for linear amplitude $\sigma_8 \gtrsim 0.5$ because the simulations produce too many massive halos compared with the observations. The simulations also produce too many low-mass halos. The distribution of halos characterized by their circular velocities for the P^3M simulations is in reasonable agreement with the observations for 150 km s^{-1} $\lesssim V_{\rm circ} \lesssim$ 350 km s^{-1}.

Subject headings: cosmology: theory — dark matter — galaxies: structure — methods: numerical

1. INTRODUCTION

This paper is part of a two-part series testing the cold dark matter (CDM) model of galaxy formation assuming a critically closed universe, $\Omega = 1$. These papers focus on the formation and clustering of halos in cosmologically significant volumes of space (cubes of length $\gtrsim 50$ Mpc on a side) with sufficient mass resolution and length resolution (force softening and box size) to resolve thousands of individual halos. The goal is not to study large-scale structure ($\gtrsim 200$ Mpc; e.g., Park 1990). Rather, the goal is to study spatial and velocity statistics on scales ~ 1–10 Mpc using candidate galaxy halos identified in the nonlinear, evolved density field. A principal goal of both papers is to determine if there exists a linear normalization of the initial fluctuation power spectrum (a free parameter in the theory) that satisfies observational constraints on glaxy masses, clustering, and velocities, and galaxy cluster multiplicity functions.

The principal goal of *this* paper is to understand the properties of dark halos that form in cosmologically significant volumes of space in the CDM model. Specifically, we want to understand the sensitivity of halo formation and halo properties to numerical resolution. We identify which properties of halo formation (e.g., distributions of halo mass and circular velocity) are particularly sensitive to such parameters as box size, force resolution, mass resolution, and methods for identifying halos.

Other workers have studied the formation of dark halos in the CDM scenario in volumes of space much greater than (100 Mpc)^3 by using approximate methods for identifying galaxies as individual particles (e.g., Davis et al. 1985). Still others have studied volumes of space much smaller than (100 Mpc)^3 with relatively high mass and force resolution (e.g., Frenk et al. 1988). Small volumes of space do not contain long wavelengths in the initial conditions which *may* affect halo formation (studied in this paper) and which *do* affect clustering (Gelb & Bertschinger 1994, hereafter Paper II). The larger volumes of space simulated with relatively high numerical resolution presented in this paper also yield better statistics since more halos form than in smaller volumes.

From our efforts, based on over 1000 IBM 3090 supercomputer-hours applied to more than a dozen large simulations, we gain insight into dynamic range by systematically isolating various effects. We demonstrate which halo properties, if any, converge with increasing resolution up to practical limits using present-day supercomputers. These dynamic range studies are important for future workers who need to choose a particular set of simulation parameters for a particular problem in galaxy formation.

By comparing the distribution of halo masses with estimates from observed galaxies, we show that the simulations produce too many massive halos. In Paper II, focusing on the spatial and velocity statistics of the halos, we consider the possibility that the overly massive halos represent clusters of galaxies (Katz & White 1993; Evrard, Summers, & Davis 1994). Because our simulations do not include gas dynamical dissipation, it is possible that the dark matter halos we identify have clustering properties different from the luminous galaxies that would form if we properly simulated all of the physics of galaxy formation. To minimize the uncertainty caused by our lack of dissipative physics, we try to employ tests that should not depend strongly on the relation between dark halos and luminous galaxies. For the same reason, in Paper II we explore several different prescriptions for galaxy formation and we discuss cosmological N-body simulations employing gas dynamics (e.g., Cen & Ostriker 1992a, b; Katz, Hernquist, & Weinberg 1992).

The N-body simulations follow the nonlinear gravitational clustering (in an expanding universe) of particles representing collisionless clouds of dark matter. The simulations utilize between 64^3 (262,144) and 256^3 (16,777,216) particles in a uni-

[1] Present address: NASA/Fermilab Astrophysics Center, Fermi National Accelerator Laboratory, P.O. Box 500, Batavia, IL 60510.

verse with $\Omega = 1$ and $H_0 = 50$ km s^{-1} Mpc^{-1}. All distances are given in units Mpc rather than h^{-1} Mpc. Most of the simulations are computed in cubes of length 51.2 Mpc on a side (box sizes are comoving). As we show in Paper II, this volume is too small to accurately measure galaxy clustering, although it allows one to resolve thousands of individual halos with hundreds to thousands of particles per typical Milky Way–sized halo. (We do, however, compute a few simulations in boxes of order 100 Mpc on a side in order to study galaxy clustering and small-scale peculiar velocities in Paper II.)

Our simulations employ both the particle-mesh (PM) method (Hockney & Eastwood 1982) and the adaptive particle-particle–particle-mesh (P^3M) method (Couchman 1991). For a review of N-body methods in cosmology see Bertschinger (1991). Bertschinger & Gelb (1991) provide an overview of the numerical aspects of this work. Gelb (1992) provides many technical details and is the basis of these papers.

In the remainder of this Introduction we discuss briefly three key issues relevant for cosmological simulations of galaxy halo formation: force resolution, halo identification, and the normalization of the power spectrum. In § 2 we use the cumulative mass fraction of halos to study the effects of numerical resolution on halo formation, and we compare the simulations with the Press-Schechter (1974) theory. In § 3 we explore circular velocity profiles and introduce observational data. In § 4 we compare the number of halos, characterized by their circular velocities, with observations. Separate subsections are included for high-mass halos and for low-mass halos. Conclusions and a summary are given in § 5.

1.1. *Force Resolution*

An important ingredient in N-body simulations is force resolution. We characterize the force softening in the simulations (with particle mass $m_{\rm part}$) by the comoving pair separation $r = R_{1/2}$ such that $r^2F_r/(Gm_{\rm part}^2) = \frac{1}{2}$, i.e., where the radial component of the force between two particles is half its Newtonian value. For the PM simulations $R_{1/2} \approx 1.4$ grid cells (Gelb 1992, chap. 2). For P^3M simulations with a Plummer force law characterized by a softening ϵ, i.e., with $F_r = Gm_{\rm part}^2 r/(r^2 + \epsilon^2)^{3/2}$, $R_{1/2} \approx 1.305\epsilon$. The shape of the PM softening is slightly different from a Plummer law, but in each case the appropriate force law (inverse square or Plummer) is matched accurately (to better than 2% rms) for $r > 2R_{1/2}$. There is, in addition, a small transverse component of the force due to PM grid anisotropies. Force errors are minimized using a suitable Green's function; see Bertschinger (1991), Gelb (1992), and Hockney & Eastwood (1982).

For economy of notation and ease of reference we refer to the simulations as follows: CDM $n(N, L, R_{1/2})$. Following Gelb (1992), we number the simulations from $n = 1$–16. The numbers in parentheses indicate the following simulation parameters: (1) N particles, (2) a comoving box of length L Mpc on a side, and (3) a comoving force softening length of $R_{1/2}$ kpc. For example, CDM 1 (128^3, 51.2, 280) uses 128^3 particles, a (51.2 Mpc)^3 box, and a comoving force softening length of 280 kpc. The two P^3M simulations discussed in these papers use $R_{1/2} = 52$ kpc comoving ($\epsilon = 40$ kpc) and $R_{1/2} = 85$ kpc comoving ($\epsilon = 65$ kpc). The other simulations are low force resolution PM simulations with $R_{1/2} \geq 190$ kpc comoving.

We summarize the simulation parameters in Table 1. The entries are the following: simulation number, particle-mesh grid, particle mass, starting expansion factor, number of time-steps to $\sigma_8 = 1$, energy conservation relative to change in gravitational potential energy (see Gelb 1992, chap. 2), computer hours consumed, initial conditions identifier. Simulations with the same initial conditions identifier use equivalent sets of random numbers, i.e., they are generated from the same set of random numbers scaled to the appropriate power spectrum (see Gelb 1992, chap. 3).

We use a time-centered leapfrog scheme (Hockney & Eastwood 1982) to advance the particles. All of the simulations are integrated using equal steps in expansion factor a, except CDM 12, which uses equal steps in a^α with $\alpha = 0.5$, as highlighted, for example, in the notable features column.

All of the simulations use cloud-in-cell (CIC, see Hockney & Eastwood 1982) interpolation and a Holtzman (1989) CDM transfer function with 5% baryons, except CDM 16, which uses triangular-shaped-cloud (TSC, see Hockney & Eastwood 1982) interpolation and a Bardeen et al. (1986, hereafter BBKS) transfer function.

In order to avoid interference between the initial interparticle lattice and the PM grid (see Gelb 1992, chap. 2), we begin CDM 6 with extra soft forces (i.e., we set the particle shape to be a linear sphere density profile with radius $\eta = 5$ grid cells, see Gelb 1992, Appendix I; then we set $\eta = 3.5$ grid

TABLE 1

SIMULATIONS

CDM $n(N, L, R_{1/2})$[a]	Grid	$m_{\rm part}$[b]	a_s[c]	$N_{\rm steps}$	EC[d]	HRS	IC Number	Notable Features
CDM 1(128^3, 51.2, 280)	256^3	4.4	0.017	500	2.4	25	1	
CDM 2(128^3, 51.2, 280)	256^3	4.4	0.017	500	2.6	22	2	
CDM 3(128^3, 51.2, 280)	256^3	4.4	0.017	500	2.6	22	3	
CDM 4(128^3, 51.2, 280)	256^3	4.4	0.018	500	2.3	22	4	
CDM 5(128^3, 51.2, 280)	256^3	4.4	0.015	500	2.5	22	5	
CDM 6(256^3, 51.2, 190)	384^3	0.55	0.014	800	14.0	180	1	High mass resolution
CDM 7(64^3, 51.2, 280)	256^3	35.2	0.024	500	1.1	19	1	Poor mass resolution
CDM 8(64^3, 51.2, 560)	128^3	35.2	0.024	200	2.2	1	1	Poor force & poor mass resolution
CDM 9(128^3, 51.2, 280)	256^3	4.4	0.024	500	2.1	22	1	Initial conditions from 64^3
CDM 11(128^3, 102.4, 560)	256^3	35.2	0.021	500	1.2	22	2	Poor force resolution; $L = 102.4$ Mpc
CDM 12(64^3, 51.2, 52)	256^3	35.2	0.024	2000	17.0	100	1	$\epsilon = 40$ kpc; $\alpha = 0.5$; Poor mass resolution
CDM 16(144^3, 100, 85)	420^3	23.0	0.014	1200	5.1	770	6	$\epsilon = 65$ kpc; $L = 100$ Mpc; TSC; BBKS

[a] Number of particles, comoving box size (Mpc), and comoving softening scale (kpc): $R_{1/2}^2 F/(Gm_{\rm part}^2) = \frac{1}{2}$.
[b] Particle mass, units of $10^9 M_\odot$.
[c] Starting expansion factor with $a = 1$ when $\sigma_8 = 1$.
[d] Energy conservation, $|\Delta C/\Delta(aU)|/10^{-4}$, i.e., change in energy constant relative to gravitational energy.

cells after the initial lattice disappears.) For CDM 16, with 144^3 particles, we use a 288^3 grid (we use a 420^3 grid after $a = 0.7$).

High force resolution in a cosmologically significant box ($\gtrsim 50$ Mpc) is computationally challenging but can lead to significantly different results compared with low-resolution simulations. One of our principal goals is to study the properties and clustering of resolved halos, so we are forced to compromise mass and force resolution by using up to 100 Mpc boxes. Other authors interested in the detailed properties of halos, and not clustering, have concentrated their efforts on very small box sizes. For example, Warren et al. (1991) used a tree code to simulate the formation of halos with very high particle number (1,097,921 particles) and very high force resolution (Plummer softening of 5 kpc proper) in a sphere of radius 5 Mpc. In another work, Dubinski & Carlberg (1991) studied CDM halo properties using a tree code with 32^3 particles in a sphere of radius 2.3 Mpc. The initial conditions were generated in a 8 Mpc box. The authors used an approximate treatment of tidal fields and a Plummer softening of 1.4 kpc. In the present paper the goal is to understand properties of halos evolved in larger boxes but with mass and force resolution significantly better than earlier efforts in boxes exceeding ~ 50 Mpc (e.g., Davis et al. 1985; White et al. 1987; Carlberg & Couchman 1989; Melott 1990; Park 1990).

1.2. *Halo Identification*

The standard method for identifying halos from the evolved particle positions is to identify all particles within a given linking distance of each other (the friends-of-friends or FOF algorithm). We developed an alternative, novel procedure that identifies local density maxima in the smoothed, evolved density field: DENMAX (see Bertschinger & Gelb 1991; Gelb 1992, chap. 4). We first compute a static density field $\delta\rho/\rho$ by interpolating the particles onto a grid. We then move the particles according to the equation

$$\frac{d\boldsymbol{x}}{d\tau} = \nabla \frac{\delta\rho}{\rho}, \tag{1.1}$$

using a ficticious time variable τ with $\delta\rho/\rho$ held constant throughout the calculation. This equation describes a viscous fluid subject to a force proportional to the density gradient, in the limit of large damping. Every particle moves toward a density maximum where it comes to rest. All particles lying within closed density contour surfaces around a peak are pushed toward that peak. After the particles are sufficiently concentrated at density peaks, the particles are scooped up and their labels are recorded. A halo is composed of these particles with their original positions restored. The results of DENMAX depend on the degree of smoothing used to define the density field $\delta\rho/\rho$. We use trilinear (CIC) interpolation with a given grid (e.g., 512^3 or smaller for sensitivity tests) to define the density field.

After identifying halos, we remove the unbound particles, treating each halo in isolation. We compute the potential for each particle i, ϕ_i, due to all N_h members of a halo:

$$\phi_i = \sum_{\substack{j=1 \\ (j\neq i)}}^{N_h} \phi(r_{ij}); \quad r_{ij} = |\boldsymbol{r}_j - \boldsymbol{r}_i| . \tag{1.2}$$

The potential is computed once and is fixed throughout the calculation. [For the P^{3}M simulations we simply use the potential $\phi(r) = -Gm/(r^2 + \epsilon^2)^{1/2}$. For the PM simulations we generate $\phi(r)$ by integrating a force table generated by Monte Carlo sampling the PM force between pairs of particles.] We then iteratively remove unbound particles as follows. We compute the energy $E_i = (1/2)m|\boldsymbol{v}_i - \boldsymbol{v}_{\rm cm}|^2 + \phi_i$ for each particle i, where $\boldsymbol{v}_{\rm cm}$ is the mean velocity of the bound particles at any given stage. We then remove all particles with $E_i > 0$. The procedure is repeated, each time recomputing $\boldsymbol{v}_{\rm cm}$, until no more particles are removed. In all of the DENMAX analyses we remove the unbound particles. We have also identified halos using the FOF algorithm *without* the removal of unbound particles.

1.3. *Normalization of the Spectrum*

Most of the simulations are analyzed assuming three normalizations of the initial, linear CDM power spectrum (a free parameter in the theory). We define the normalization factor σ_8 using a top-hat sphere of radius $8\ h^{-1}$ Mpc:

$$\sigma_8^2 \equiv \int_0^\infty d^3k P_{\rm lin}(k) W_{\rm TH}^2(kR); \quad R = 8\ h^{-1}\ {\rm Mpc} \tag{1.3}$$

with the top-hat filter defined as

$$W_{\rm TH}(kR) = \frac{3}{(kR)^3}(\sin kR - kR\cos kR) \tag{1.4}$$

for comoving wavenumber k. The linear power spectrum of density fluctuations is

$$P_{\rm lin}(k) = \lim_{a_i \to 0} a_i^{-2} P(k, a_i) . \tag{1.5}$$

To define the CDM power spectrum we use the primordial scale-invariant spectrum modulated by the transfer function computed by BBKS or by Holtzman (1989) with 5% baryon fraction. The difference between the two is very small except at high wavenumbers. We normalize the initial spectrum according to equation (1.3) with expansion factor $a \equiv 1$ when $\sigma_8 = 1$. We then scale the fluctuations to some early time a_i using linear theory, i.e., $P(k, a_i) = a_i^2 P(k, a = 1)$.

We generally apply linear theory until the largest $|\delta\rho/\rho|$ on the initial particle grid is unity. For the 144^3 particle simulation CDM 16, however, linear theory is applied until the largest three-dimensional displacement is one mean interparticle spacing, i.e., $L/N^{1/3}$ for box size L and N particles. The Zel'dovich (1970) approximation is used to get particle positions and velocities at the end of the linear regime. The system is then evolved using the N-body code, with particle positions and velocities recorded at various expansion factors $a = \sigma_8$. (By definition, $\sigma_8 \propto a$.) In most cases we study the models at $\sigma_8 = 0.5$, 0.7, and 1.0. In the literature, for example, $\sigma_8 = 0.4$ is known as the $b = 2.5$ biased CDM model because of the assumption that galaxy density fluctuations are 2.5 times the mass density fluctuations. According to the linear biasing paradigm, $b = 1/\sigma_8$. We do not adopt the linear biasing paradigm because we prefer to identify halos in the nonlinear, evolved mass distribution. Note that according to our prescription, the variance of halo numbers in $8\ h^{-1}$ Mpc spheres does not necessarily equal σ_8. The *COBE* measurements of microwave background anisotropy imply (for a scale-invariant spectrum of density perturbations and the standard CDM transfer function) $\sigma_8 \approx 1.1$ (Wright et al. 1992; Efstathiou, Bond, & White 1992; Adams et al. 1993).

2. DYNAMIC RANGE: CUMULATIVE MASS FRACTIONS

In this section we discuss distributions of halos using the cumulative mass fraction (CMF).

2.1. *The CMF*

The CMF is defined by

$$\mathrm{CMF}(M) = \frac{1}{N} \sum_{M'=M}^{\infty} n(M')M' , \qquad (2.1)$$

where N is the total number of particles in the simulation, M is the mass (number of particles) of a halo, and $n(M)$ is the number of halos containing M particles. By definition, $\mathrm{CMF}(0) = 1$, $\mathrm{CMF}(\infty) = 0$, and $\mathrm{CMF}(M)$ is a decreasing function of M. Note that the particle mass for N particles in a cube of comoving size L is

$$m_{\mathrm{part}}(N, L) = 4.44 \times 10^9 \, M_\odot \left(\frac{128^3}{N}\right)\left(\frac{L}{51.2 \text{ Mpc}}\right)^3 . \qquad (2.2)$$

The CMF gives the fraction of mass contained in halos more massive then M. Although the number and masses of large halos can fluctuate significantly from simulation to simulation, their contribution to the CMF gets averaged in the sum of equation (2.1). The smallest mass taken is typically five or more particles. The CMF has the advantage of summarizing in a nondimensional way all information about the mass function of halos. However, it has the disadvantage that halo masses are not easy to compare with observations. Also, because halos do not have sharp outer boundaries, the total mass of a given halo is often not a well-defined quantity. We address these problems later by applying a radial cutoff in order to compare with observations. Here the motives are purely theoretical in order to understand the effects of finite resolution.

The first issue we study using the CMF is the difference between halos identified using DENMAX versus FOF. Figure 1 shows the cumulative mass fraction versus mass for halos found in CDM 1(128^3, 51.2, 280) analyzed with DENMAX and FOF($l = 0.1$) and FOF($l = 0.2$), where l is the linking parameter in units of the mean interparticle spacing. The DENMAX masses include only the bound particles, while the FOF masses include all of the identified particles. The DENMAX CMFs lie between the FOF CMFs for $l = 0.1$ and $l = 0.2$. A smaller FOF linking parameter leads to smaller halos, but also to a smaller fraction of particles in halos. The reason for this is that FOF includes only particles such that the local overdensity exceeds $\sim 2l^{-3}$. DENMAX, however, gathers all particles around a peak, even those at lower density. FOF with $l = 0.1$ dissolves low-density halos. If l is increased, then FOF merges halos together, increasing the maximum masses, even when the halos have distinct substructure (see Gelb 1992, chap. 4, and Fig. 18 below). DENMAX avoids this problem: basically, any density concentration visible graphically will be found by DENMAX. (Indeed, graphical tests were first used to establish and test the algorithm.) Note that more than half of the particles are associated with *some* DENMAX halo, even at early times. This is the natural outcome of gravitational instability in a model with small-scale structure. Contrary to some expectations, most of the CDM is not smoothly distributed.

Although the differences in the CMF obtained using DENMAX and FOF are large, total halo masses are not measured in practice. It remains to be seen whether or not observable differences between DENMAX and FOF halos are large,

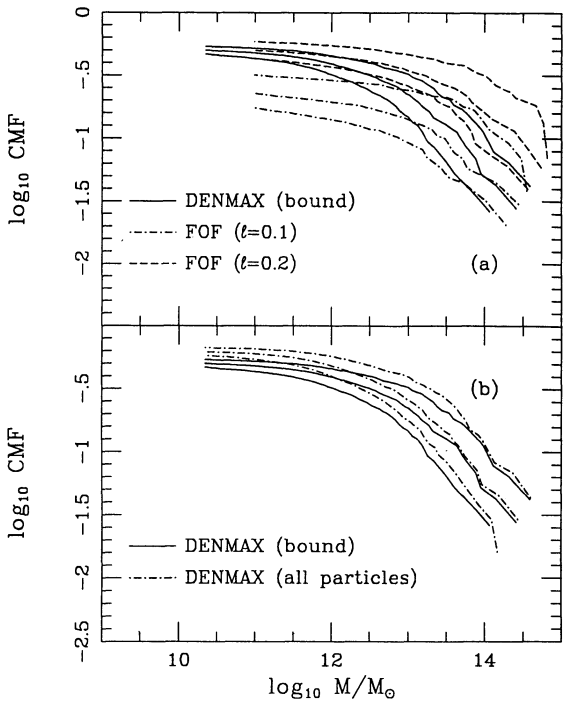

FIG. 1.—Cumulative mass fractions for CDM 1(128^3, 51.2, 280) analyzed using FOF($l = 0.1$), FOF($l = 0.2$), and 512^3 DENMAX. (*a*) Compares DENMAX (*solid curves*) with FOF (*dot-dashed curves* for $l = 0.1$; *dashed curves* for $l = 0.2$) and (*b*) the effect of the removal of unbound particles (*solid curves* for bound particles; *dot-dashed curves* for all particles). Each case has three curves—*lower curves* ($\sigma_8 = 0.5$), *middle curves* ($\sigma_8 = 0.7$), and *upper curves* ($\sigma_8 = 1$).

and whether the results depend on the DENMAX grid or on l. DENMAX has a limitation stemming from the arbitrary choice of a density grid (512^3 for most of the analysis) or equivalently a smoothing scale for defining the density field. (Similarly, FOF has its own arbitrary parameter, l.) We explore these issues later. For now, our prejudice is to favor DENMAX because it does not suffer from the obvious defects of FOF, the dissolving of low-density halos and the merging of halos in high-density regions. We include FOF analysis only for comparison with DENMAX because many authors use FOF (e.g., White et al. 1987; Carlberg, Couchman, & Thomas 1990; Brainerd & Villumsen 1992).

The lower panel in Figure 1 shows the effect of the removal of unbound particles. The unbinding process systematically reduces the mass of the halos over the full range of masses, although the effects are largest for small masses. We find that the DENMAX results without the removal of unbound particles are in better agreement with $l = 0.2$ FOF. However, the agreement is not exact; we show later that FOF occasionally links together visually distinct halos. Moreover, unbound particles are temporary members of the halos and therefore should not be included.

Is there a significant simulation-to-simulation variation in the CMF? In Figure 2 we show cumulative mass fractions for five simulations. They are all 128^3 particle PM simulations (with $R_{1/2} = 280$ kpc comoving) computed in 51.2 Mpc boxes using different initial random numbers. There is very little scatter at the low-mass end and there is considerable scatter at the high-mass end. The fluctations at the high-mass end are

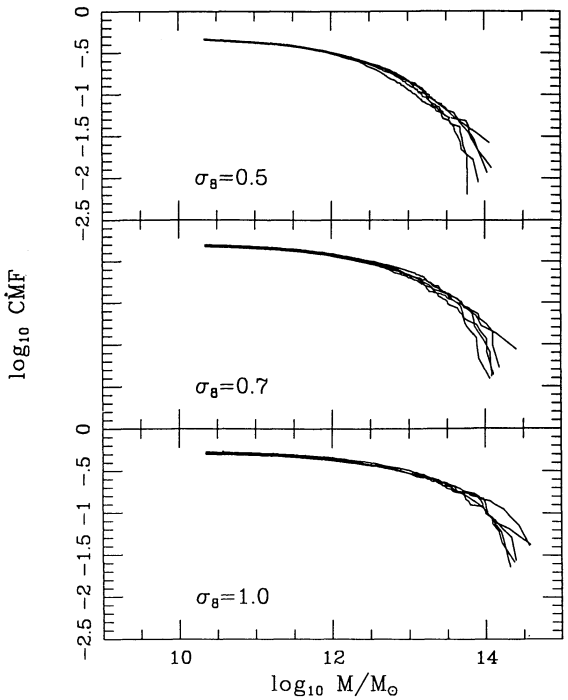

FIG. 2.—Cumulative mass fractions for 512^3 DENMAX halos from CDM 1–5. All use 128^3 particles, a 51.2 Mpc box, and a force softening distance $R_{1/2} = 280$ kpc comoving.

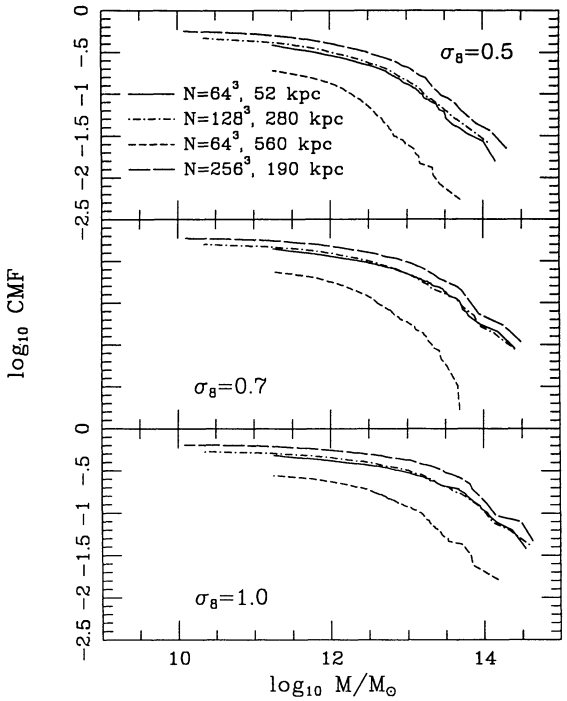

FIG. 3.—Cumulative mass fractions for 512^3 DENMAX halos from various simulations in 51.2 Mpc boxes. The effects of particle number, N, and force softening, $R_{1/2}$, are shown. All four simulations are generated from an equivalent set of random numbers.

due to small number statistics in these small volumes. We conclude that the CMF is not sensitive to simulation-to-simulation fluctuations except for rare massive halos.

The next important issue is the effect of varying mass resolution and force resolution. In Figure 3 we attempt to determine these effects by comparing four simulations in 51.2 Mpc boxes which use initial conditions taken from an equivalent set of initial random numbers. (The same values are used for the initial Fourier transform of the density fluctuation field for all wavenumbers up to the Nyquist frequency for each cube. Thus the initial conditions for $N = 128^3$ are identical to those for $N = 64^3$ except that extra high-frequency power is present with the larger number of particles.) Mass and force resolution variations cause several effects that we systematically separate out as we proceed.

The $N = 64^3$, $R_{1/2} = 560$ kpc comoving PM simulation fails to match up with the other simulations—this is not surprising considering that the force softening is so poor, larger than the size of many halos. The two very different simulations (the P^3M simulation with 64^3 particles and $R_{1/2} = 52$ kpc comoving vs. the PM simulation with 128^3 particles and $R_{1/2} = 280$ kpc comoving) surprisingly yield very similar CMFs, but the harder forces in the P^3M simulation actually give rise to halos with higher circular velocities, an important effect that is discussed in § 4. (We show as we proceed that the similarity of the CMF for these two simulations occurs because increased mass resolution and increased force resolution both increase the CMF.) The 256^3 particle simulation lies above the others due to the increase in mass resolution and the presence of more small-scale power in the initial conditions.

2.2. *DENMAX Resolution and Box Size*

We need to understand what happens if we vary the DENMAX grid when analyzing the same simulation. In Figure 4 we show the results of several DENMAX analyses of the P^3M simulation CDM 12(64^3, 51.2, 52) at $\sigma_8 = 0.5$. We see that the DENMAX grid significantly influences the CMF. This variation is analogous to the variation of the CMF with linking length l for the FOF algorithm (cf. Fig. 1). We demonstrate later, however, that the circular velocities of the halos are less sensitive to the DENMAX grid—this is because circular velocities involve using a cutoff distance from the local density maximum. One effect arising from different DENMAX grids is the inclusion of distant particles into the halos. We demonstrate later that the DENMAX grid influences the break-up of massive halos when the grids are coarser than the force resolution of the simulation itself. Because of the density grid sensitivity of DENMAX, particularly for the total number of bound particles, we must compare the CMF from different simulations using the same effective DENMAX resolution.

Are there significant differences in the CMF computed in boxes larger than 51.2 Mpc? In Figure 5 we show the CMF for

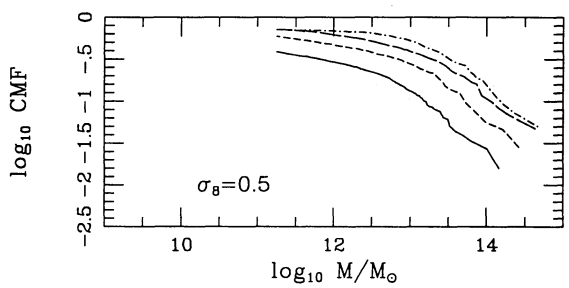

FIG. 4.—Cumulative mass fractions at $\sigma_8 = 0.5$ for DENMAX halos from CDM 12(64^3, 51.2, 52) using a 512^3 grid (*solid curve*), and lower resolution DENMAX grids: 256^3 grid (*short-dashed curve*); 128^3 grid (*long-dashed curve*); and 64^3 grid (*dot-dashed curve*).

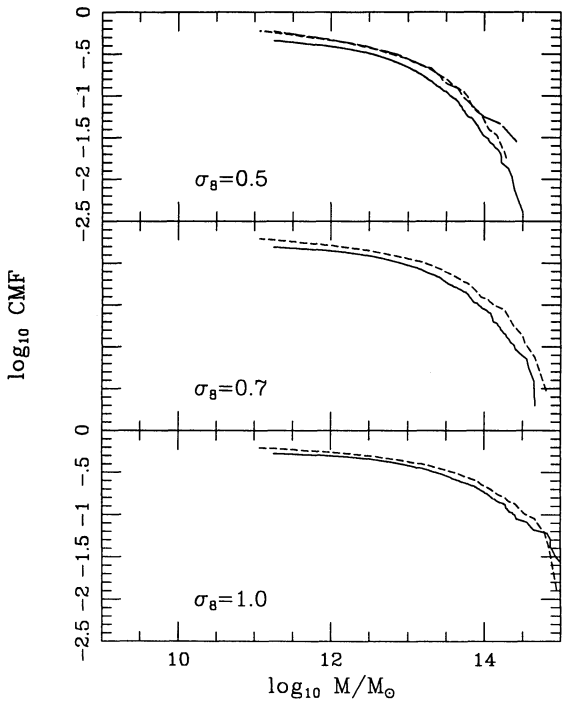

FIG. 5.—Cumulative mass fraction for 512^3 DENMAX halos from two simulations in bigger boxes: CDM 11(128^3, 102.4, 560; *solid curves*) and CDM 16(144^3, 100, 85; *short-dashed curves*). Also, top panel ($\sigma_8 = 0.5$) for 256^3 DENMAX halos from CDM 12(64^3, 51.2, 52; *long-dashed curve*).

two simulations computed in larger boxes (102.4 Mpc and 100 Mpc). Since we also use a 512^3 DENMAX grid for these simulations, the DENMAX resolution is only roughly half the resolution of the 51.2 Mpc simulations analyzed with a 512^3 DENMAX grid. The difference is significant (cf. Kundić 1991). In order to separate out the effects due to larger waves in the initial conditions for the 100 Mpc boxes, compared with 51.2 Mpc boxes, we compare CDM 16(144^3, 100, 85) analyzed with a 512^3 DENMAX grid with CDM 12(64^3, 51.2, 52) analyzed with a 256^3 DENMAX grid. (This is done at $\sigma_8 = 0.5$ only.) The two simulations, CDM 16 and CDM 12, have comparable force resolution ($R_{1/2} = 85$ kpc comoving and 52 kpc comoving, respectively) and comparable mass resolution ($m_{\rm part} = 2.3 \times 10^{10}\ M_\odot$ and $3.5 \times 10^{10}\ M_\odot$, respectively). The nearly perfect agreement between CDM 16 (100 Mpc box) analyzed with 512^3 DENMAX and CDM 12 (51.2 Mpc box) analyzed with 256^3 DENMAX and the fact that the two simulations have comparable force and mass resolution indicate that longer waves in the initial conditions do not significantly affect halo formation. (However, some of the longer waves have not gone nonlinear yet at $\sigma_8 = 0.5$.) This is encouraging because it means we can use the simulations in 51.2 Mpc boxes to understand halo properties. We will discover in Paper II, however, that the velocity dispersion of pairs of halos is significantly influenced by the different box sizes.

To quantify the sensitivity of the CMF to DENMAX resolution, we measure the mass where the CMF equals 20%, denoted as M_{20}. We choose 20% because larger values are not well spanned by the various simulations and smaller values are more sensitive to the simulation-to-simulation variations of the massive halos. We compute, for CDM 12(64^3, 51.2, 52) at $\sigma_8 = 0.5$, the logarithmic slope $\Delta \log M_{20}/\Delta \log D$, where D is the DENMAX grid spacing. In Figure 4, comparing a 512^3 DENMAX with a 256^3 DENMAX analysis, we estimate $\Delta \log_{10} M_{20} \approx 12.65\text{–}13.33 = -0.68$ and $\Delta \log_{10} D = \log_{10}(1/2)$ so $\Delta \log M_{20}/\Delta \log D \approx 2.27$. Increasing D decreases the DENMAX resolution, thereby increasing the CMF. This is because a coarser DENMAX grid tends to pick out larger masses, i.e., it cannot resolve substructure. Comparing a 256^3 DENMAX grid with a 128^3 DENMAX grid we find $\Delta \log M_{20}/\Delta \log D \approx 1.13$. Comparing a 128^3 DENMAX grid with a 64^3 DENMAX grid we find $\Delta \log M_{20}/\Delta \log D \approx 0.57$. We therefore see evidence for increasing amounts of substructure on smaller scales. Qualitatively similar behavior occurs with the FOF algorithm (cf. Fig. 1), where the linking parameter plays the role of the resolution scale. We demonstrate later that if we impose a radial cut on the DENMAX halos, as we do when we study circular velocities, the results are not as sensitive to resolution.

2.3. *Small-Scale Waves*

Figure 6 is important for understanding the effect of varying the number of particles—particularly for separating out the fact that increasing the particle number not only increases the mass resolution, but it also probes smaller fluctuations in the initial power spectrum because of the higher Nyquist wavenumber cutoff. In a discrete system with N particles, the highest wavenumber represented is $(2\pi/L)(N^{1/3}/2)$ in each dimension. We show the results of a 512^3 DENMAX analysis from three $R_{1/2} = 280$ kpc comoving PM simulations in 51.2 Mpc boxes which use equivalent initial conditions. The results are shown at three epochs for 128^3 and 64^3 particles. We also ran a simulation (CDM 9) using 128^3 particles, but the initial conditions are generated by interpolating the 64^3 particle case to 128^3 particles. Therefore, this simulation has the same mass resolution as the noninterpolated 128^3 particle simulation (CDM 1) but does not have the small-scale waves present in the noninterpolated simulation.

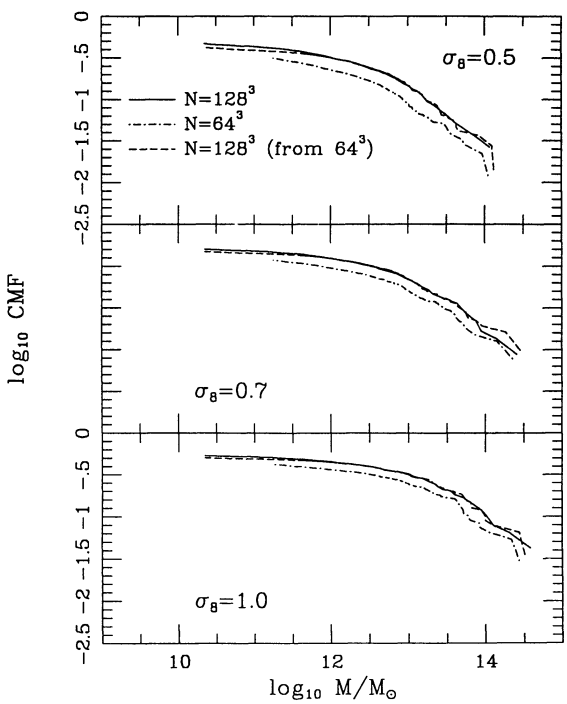

FIG. 6.—Cumulative mass fractions for 512^3 DENMAX halos from three $R_{1/2} = 280$ kpc comoving PM simulations in 51.2 Mpc boxes. All three simulations use equivalent initial conditions. The dashed curves are for 128^3 particles—*but* the initial displacements were interpolated from the 64^3 particle case (*dot-dashed curves*).

Apart from the obvious increase in the CMF due to an increase in mass resolution (explored in greater detail below), we see in Figure 6 the effect of the small-scale waves in the initial conditions—the noninterpolated 128^3 particle simulation has a higher value of the CMF at small mass relative to the interpolated 128^3 particle case but not by much. Little, Weinberg, & Park (1991) studied the effect of the removal of high-frequency waves in scale-free models. Using a PM simulation with 128^3 particles and $P(k) \propto k^{-1}$, they found that the nonlinear power spectrum in a simulation with initial power above $kL/(2\pi) = 32$ set to zero compared very well with the nonlinear power spectrum in a simulation with initial power above $kL/(2\pi) = 64$ set to zero. Only small differences appeared on small scales, but further reductions in the initial cutoff frequency did produce large effects.

2.4. *Separation of Effects*

We now separate out the effects of mass and force resolution bearing in mind that (1) we need to compare simulations in boxes of different sizes with the same effective DENMAX resolution; (2) the differences in the CMF arising from the inclusion of extra high- and low-frequency waves in the initial conditions are small; and (3) the simulation-to-simulation (i.e., different initial random numbers) differences in the CMF are small below about 10^{13} $M_\odot$. To separate out effects of resolution we reexamine Figures 3 through 6.

We first demonstrate that higher mass resolution increases the CMF. If we examine Figure 6 we see that the CMF is higher for the $N = 128^3$ particle simulation than for the $N = 64^3$ particle simulation using the same force resolution ($R_{1/2} = 280$ kpc comoving in a 51.2 Mpc box). Comparing 128^3 and 64^3 particle simulations, we find $\Delta \log M_{20}/\Delta \log m_{\rm part} \approx -0.56$. The minus sign reflects the fact that if the particle mass increases, then the mass resolution $\propto 1/m_{\rm part}$ decreases, and therefore M_{20} (or equivalently the CMF) decreases. The higher mass resolution simulations lead to a higher value of the CMF independent of force resolution. We also see this in Figure 3 by comparing the 256^3 particle simulation ($R_{1/2} = 190$ kpc comoving in a 51.2 Mpc box) with the 128^3 particle simulation ($R_{1/2} = 280$ kpc comoving in a 51.2 Mpc box). The difference between $R_{1/2} = 190$ kpc comoving and $R_{1/2} = 280$ comoving is shown later to have a nontrivial effect on the CMF.

For the 256^3 particle simulation we find $\log_{10} M_{20} \approx 13.05$ and for the 128^3 particle simulation we find $\log_{10} M_{20} \approx 12.74$. Therefore, we find $\Delta \log M_{20}/\Delta \log m_{\rm part} \approx -0.34$. The effect on the CMF (logarithmic slope) is smaller going from 256^3 to 128^3 particles (-0.34) compared with going from 128^3 to 64^3 particles (-0.56), but it is not obvious if and when the results will converge.

The fact that increased mass resolution continues to increase the CMF in the above comparisons warrants further investigation. Is this result still true when we impose a distance cut from the density peak? We reanalyze the three PM simulations (64^3, 128^3, and 256^3 particles) at $\sigma_8 = 0.5$ imposing a distance cut of 300 kpc comoving from the density peak. The results are shown in the top panel of Figure 7. In all three cases we do not remove the unbound particles from halos with raw masses (no cut in radius and no unbinding) exceeding 1.1×10^{13} $M_\odot$ (location of vertical line; *the transition mass*) to be consistent with the analysis of the 256^3 particle simulation. (In all the analyses of the 256^3 particle simulation CDM 6 we do not remove the unbound particles from the massive halos,

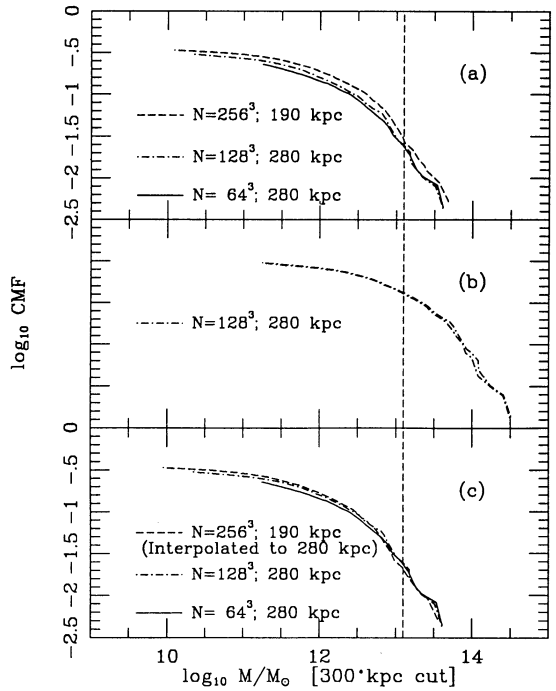

FIG. 7.—Cumulative mass fractions for 512^3 DENMAX halos at $\sigma_8 = 0.5$ from three PM simulations using equivalent initial conditions. We include only particles within 300 kpc comoving from the density peak. (*a*) Compares three simulations indicated by particle number N and force softening $R_{1/2}$. The halos whose raw mass (no cut in radius and no unbinding) exceeding the transition mass (1.1×10^{13} $M_\odot$; vertical bar) have not had their unbound particles removed. (*b*) Results with and without the removal of unbound particles above the transition mass. (*c*) The same curves from Fig. 7*a* except the 256^3 particle, $R_{1/2} = 190$ kpc comoving simulation has been scaled to $R_{1/2} = 280$ kpc comoving.

$M \geq 1.1 \times 10^{13}$ $M_\odot$, because it is computationally prohibitive.) However, the unbinding of the massive halos has a small effect on the CMF below the transition mass. To see this, we show in the middle panel of Figure 7 at $\sigma_8 = 0.5$ the CMF from the 64^3 particle simulation and from the 128^3 particle simulation with and without the unbinding of the massive halos. The effect is negligible just below the transition mass, and there is a slight increase in the CMF above the transition mass.

By examining the top panel of Figure 7 we find, for the 128^3 particle simulation versus the 64^3 particle simulation, that $\Delta \log M_{20}/\Delta \log m_{\rm part} \approx -0.23$. This is less than -0.56, the result when we do not impose a cut of 300 kpc comoving from the density peak. The CMF itself changes considerably when we impose a distance cut from the density peak. However, we may adopt the position that particles at such great distances from the center of the halo should not be associated with estimated measurements of the mass of observed galaxy halos. The observed mass of individual galaxy halos at great distances, as opposed to dynamical properties inferred by the motions of stars and gas at small distances, is highly uncertain. By comparing the 256^3 particle simulation with the 128^3 particle simulation we find $\Delta \log M_{20}/\Delta \log m_{\rm part} \approx -0.22$. Again this is less than -0.34, the result when we do not impose a cut of 300 kpc comoving from the density peak.

Provided that we apply a cut in radius from the density peak, as we do when we characterize the halos by their circular velocities in the next sections, we see that the CMF is less sensitive to variations in mass resolution than when we do not impose a cut. We still do not see a convergence of the CMF

with increasing mass resolution in Figure 7*a*, *b*. However, the 64^3 particle simulation and the 128^3 particle simulation both use $R_{1/2} = 280$ kpc comoving. The 256^3 particles simulation uses $R_{1/2} = 190$ kpc comoving. So next we correct for the difference in force resolution, but first we demonstrate that higher force resolution also increases the CMF.

In order to see the effect of force resolution we compare simulations with similar mass resolution. In Figure 5 we compare CDM 12(64^3, 51.2, 52) analyzed with a 256^3 DENMAX grid and CDM 11(128^3, 102.4, 560) analyzed with a 512^3 DENMAX grid. The mass resolution and the DENMAX grid resolution are equivalent since the CDM 11 box has eight times the volume of the CDM 12 box. We see that the higher force resolution simulation yields a higher value of the CMF. We find that $M_{20} \approx 13.33$ for the high-resolution simulation and 13.08 for the low-resolution simulation. If we characterize the force resolution by $R_{1/2}$, then we find that $\Delta \log M_{20}/\Delta \log R_{1/2} \approx -0.24$. This number should be treated with caution since we are comparing simulations with $R_{1/2} = 52$ kpc comoving versus $R_{1/2} = 560$ kpc comoving—this is a wide range and DENMAX behaves unreliably in very low resolution simulations. We do not have two P^3M CDM simulations with comparable mass resolution but with significantly different Plummer softenings.

The increase in CMF for higher force resolution simulations is verified by comparing CDM 12(64^3, 51.2, 52) with CDM 8(64^3, 51.2, 560) in Figure 3, but again the force resolution in CDM 8 is extremely poor.

As a final comparison of force resolution effects, we compare CDM 12(64^3, 51.2, 52) with CDM 7(64^3, 51.2, 280), both analyzed with a 512^3 DENMAX grid. We find $\Delta \log M_{20}/\Delta \log R_{1/2} \approx -0.56$. The range of force softenings in this comparison is still large but at least $R_{1/2} = 280$ kpc comoving is more reasonable than 560 kpc comoving. In subsequent sections we compare the halos characterized by their circular velocities and particular attention is paid to force resolution comparing results for PM versus P^3M simulations. So we return to force resolution then.

As a final test of the convergence of the CMF with increasing mass resolution, we first use the above force resolution analysis to estimate the effect on the CMF from a $R_{1/2} = 280$ kpc comoving PM simulation versus a $R_{1/2} = 190$ kpc comoving PM simulation. To do so, we compare the 64^3 particle, $R_{1/2} = 52$ kpc comoving P^3M simulation with the 64^3 particle, $R_{1/2} = 280$ kpc comoving PM simulation (both computed in 51.2 Mpc boxes and analyzed with a 512^3 DENMAX grid) imposing a 300 kpc comoving cut from the density peak of the halos. The logarithmic slope is $\Delta \log M_{20}/\Delta \log R_{1/2} \approx 0.74$. If we multiply -0.74 by $\Delta \log_{10} R_{1/2} = -0.18$, i.e., the difference between the softening of the $R_{1/2} = 190$ kpc comoving PM simulation and the $R_{1/2} = 280$ kpc comoving PM simulation, we get $\Delta \log_{10} M_{20} \approx 0.13$. Therefore, we can estimate that the 256^3 particle $R_{1/2} = 190$ kpc comoving PM simulation (with a 300 kpc comoving distance cut) would have $\log_{10} M_{20} \approx 11.91 - 0.13 = 11.78$ if it were computed using a $R_{1/2} = 280$ kpc comoving PM simulation.

Now if we compare the rescaled (to $R_{1/2} = 280$ kpc comoving) 256^3 particle result with the $R_{1/2} = 280$ kpc comoving 128^3 particle PM simulation, all with a 300 kpc comoving distance cut, we get $\Delta \log M_{20}/\Delta \log m_{\rm part} \approx -0.11$ compared with the old value of -0.22. This is encouraging because this logarithmic slope, -0.11, is still better than the logarithmic slope -0.23 computed earlier by comparing a 128^3 particle simulation with a 64^3 particle simulation. Graphically (as depicted in Fig. 7*c*), this corresponds to moving the CMF for the 256^3 particle simulation in the top panel of Figure 6 0.13 units to the left.

We now see that the agreement between the 128^3 particle case and the 256^3 particle case is much better (Fig. 7*c*). There is still a slight increase in the CMF on small mass scales. However, this is consistent with the fact that the 256^3 particle simulation has more small-scale power in the initial conditions compared with the 128^3 particles simulation. This effect was demonstrated earlier.

Using simulations analyzed with the same effective DENMAX resolution, we found the following. (1) Higher mass resolution leads to larger values of the CMF independent of force resolution. The effect is smaller when we impose a distance cut from the density peak of the halos. The difference between the $4.4 \times 10^9\ M_\odot$ and the $3.5 \times 10^{10}\ M_\odot$ simulation (using a distance cut of 300 kpc comoving from the density peaks of the halos) is small, $\Delta \log M_{20}/\Delta \log m_{\rm part} \approx -0.23$. The difference between the $5.5 \times 10^8\ M_\odot$ simulation and the $4.4 \times 10^9\ M_\odot$ simulation (using a 300 kpc comoving cut and correcting for the difference in force softening) is $\Delta \log M_{20}/\Delta \log m_{\rm part} \approx -0.11$. The difference has decreased in the very high mass resolution simulation indicating that convergence of the CMF with mass resolution is plausible. (2) Higher force resolution leads to larger values of the CMF independent of mass resolution. We examine the effects on the formation of halos arising from different force resolution P^3M simulations in subsequent sections. (3) Longer waves in the initial conditions (100 Mpc box vs. a 51.2 Mpc box) do not significantly affect the CMF. (4) Smaller waves in the initial conditions (64^3 particle initial conditions interpolated to 128^3 particles vs. true 128^3 particle initial conditions) do not significantly affect the CMF, aside from a small effect on small mass scales. (5) Larger DENMAX grids better resolve substructure; this lowers the CMF. The results are sensitive to the different DENMAX grids so it is important to compare CMFs using the same effective DENMAX resolution. However, we show later that the results are less sensitive when we compute circular velocities which are what we use to compare the simulated halos with the observations.

2.5. *Press-Schechter Theory*

As a final application of the CMF, we compare the simulations with the predictions of the Press-Schechter theory (Press & Schechter 1974). The Press-Schechter formalism estimates the fraction of mass in bound halos with mass greater than M to be the fraction of the mass whose linear density, averaged over a scale M, exceeds δ_c:

$$P(M) = \mathrm{erfc}\left[\frac{\delta_c}{2^{1/2}\sigma_0(M)}\right], \tag{2.3}$$

where erfc is the complementary error function. One may regard δ_c as a free parameter, although it is often taken to equal the critical overdensity for uniform spherical collapse in an Einstein–de Sitter universe, $\delta_c = 1.68$. The rms density $\sigma_0(M)$ is computed from the linear power spectrum, smoothed with an appropriate filter (window function). We use either a Gaussian window function, $W(k, R_f) = \exp(-0.5x^2)$, or a top-hat window function, $W(k, R_f) = 3(\sin x - x \cos x)/x^3$, where in both cases $x \equiv kR_f$. The generalized spectral moments (to be used below) are defined as follows:

$$\sigma_n^2(M) \equiv \int_0^\infty 4\pi k^2 P(k) W^2(k, R_f) k^{2n}\, dk\ . \tag{2.4}$$

For a Gaussian window function, the smoothing radius R_f is related to the mass as follows: $M = (2\pi)^{3/2}\rho_0 R_f^3$. For a top-hat window function, $M = (4\pi/3)R_f^3$.

Press & Schechter (1974) estimated the mass function of bound halos as $n(M)d\ln M = 2\rho_0(dP/dM)d\ln M$, where ρ_0 is the comoving background mass density. The factor of 2 is needed for normalization, but has since been derived analytically by Bond et al. (1991). The final result is

$$n(M)d\ln M = \left(\frac{2}{\pi}\right)^{1/2}\frac{\rho_0}{M}\frac{\delta_c}{\sigma_0(M)}\left|\frac{d\ln\sigma_0}{d\ln M}\right| \times \exp\left\{-\frac{1}{2}\left[\frac{\delta_c}{\sigma_0(M)}\right]^2\right\}d\ln M\,. \quad (2.5)$$

We convert equation (2.5) into a CMF using

$$\mathrm{CMF}(M) = \frac{1}{\rho_0}\int_{\ln M}^{\infty} n(M')M'\,d\ln M'\,. \quad (2.6)$$

We evaluate equation (2.6) using $\sigma_8 = 0.5$, 0.7, and 1.0 linear normalizations of the BBKS CDM power spectrum. We try $\delta_c = 1.44$ (e.g., Carlberg & Couchman 1989), $\delta_c = 1.68$ (e.g., Efstathiou et al. 1988b; Brainerd & Villumsen 1992), and $\delta_c = 2.0$, for both a Gaussian and a top-hat window function. Theoretical predictions of the Press-Schechter theory are compared with CMFs measured from the high-resolution N-body simulations CDM 12(64^3, 51.2, 52; particle mass $3.5 \times 10^{10}\ M_\odot$) and CDM 16($144^3$, 100, 85; particle mass $2.3 \times 10^{10}\ M_\odot$) in Figure 8.

First we consider the halos identified according to the FOF algorithm with a linking parameter $l = 0.2$. Figure 8*a* shows that the two simulations, at three different epochs, yield reasonably good agreement with the Press-Schechter predictions for a top-hat window function with $\delta_c = 2.0$. Only slightly worse agreement obtains with a Gaussian window function with $\delta_c = 1.68$. Note that the simulated mass distributions are broader than predicted. The high-mass tails of the distributions actually match very well the Press-Schechter predictions for a top-hat window function with $\delta_c = 1.68$, but there are fewer low-mass halos than predicted. Evidently this is because they are subsumed into more massive halos, at least with the FOF recipe, with greater efficiency than implied by the analytical model. Although the agreement with the Press-Schechter theory is not perfect, the errors do not grow with epoch; the analytical theory appears to give the correct scaling of masses as the clustering strength increases. Our result here differs from that of Brainerd & Villumsen (1992), who found the departures growing as clustering progresses.

Figure 8*b* shows similar results for a FOF linking length $l = 0.1$. Now δ_c must be increased (from 1.68 to 2.0 for the Gaussian window function) to account for the smaller masses of the halos defined at a higher overdensity. However, the agreement at small masses is significantly worsened.

Figure 8*c* shows CMFs for CDM 12(64^3, 51.2, 52) computed using DENMAX, compared with Press-Schechter theory for a Gaussian window function with $\delta_c = 2.0$. The top set of data points (*filled circles and solid curves*) are for raw DENMAX masses, with no removal of unbound particles (which would decrease the CMF by about 10%) and with no radial cut. The bottom set (*dashed curves and crosses*) have excluded unbound particles and those beyond a comoving radius of 200 kpc from the peak. There are several important things to notice. First, at early epochs, the raw DENMAX CMF agrees well with the Press-Schechter theory. At high masses the DENMAX distributions are similar to those obtained using FOF with $l = 0.1$ while at low masses they match the $l = 0.2$ case better. DENMAX breaks up the more massive clumps found with $l = 0.2$ while preserving the subclumps as individual halos.

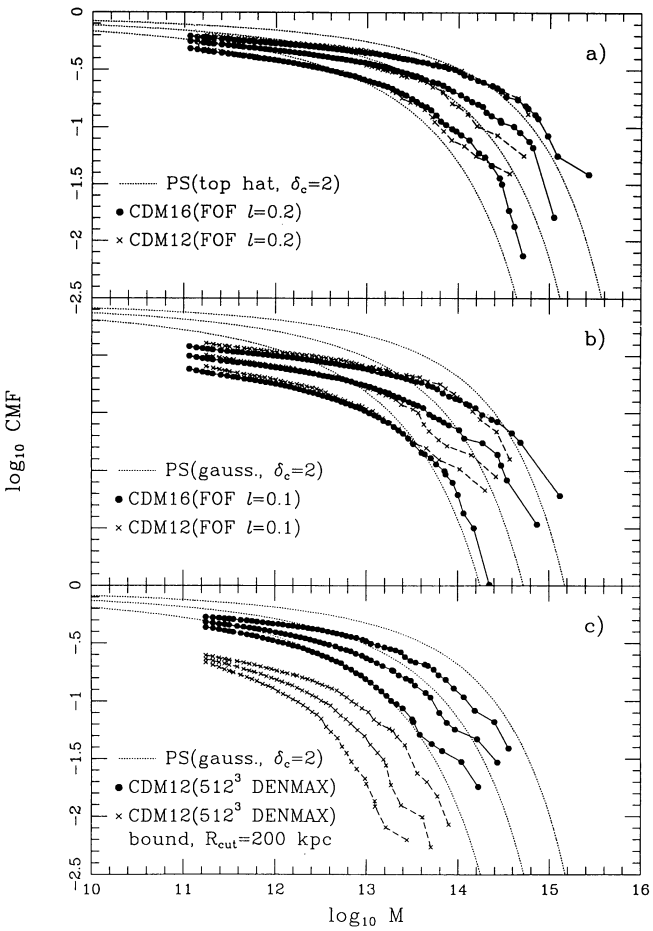

FIG. 8.—Cumulative mass fraction from CDM 12(64^3, 51.2, 52) and CDM 16(144^3, 100, 85) and the Press-Schechter theory (PS), all for $\sigma_8 = 0.5$, 0.7, and 1 with the CMF being larger with increasing σ_8. (*a*) Dotted curves are PS with a top-hat window function and $\delta_c = 2$. Solid circles are CMFs of raw masses for CDM 16 and FOF($l = 0.2$) while crosses are CMFs of raw masses for CDM 12 and FOF($l = 0.2$). (*b*) Same as (*a*) except PS is for a Gaussian window function with $\delta_c = 2$ and the simulations are CMFs of raw masses analyzed with FOF($l = 0.1$). (*c*) PS is for a Gaussian window function with $\delta_c = 2$. Solid circles are CMFs from CDM 12 computed with raw masses using a 512^3 grid DENMAX analysis. Crosses are CMFs also from CDM 12 and also computed using a 512^3 grid DENMAX analysis—however, only bound particles within 200 kpc comoving of the DENMAX peak are used to compute the CMFs.

Second, as clustering increases, the CMF grows less rapidly than the Press-Schechter prediction. This effect appears to be due to the ability of DENMAX to find substructure in halos merged by FOF. Thus, although we disagree with Brainerd & Villumsen (1992) about the results from FOF, we agree that the actual halo mass distribution grows less rapidly than predicted by Press-Schechter theory. The agreement could be improved if δ_c were to grow with epoch. In fact, at very early epochs (when there are fewer than 100 particles per group) the fit to the simulations is good with a Gaussian window and $\delta_c = 1.68$.

The third point to note from Figure 8*c* is that the radial truncation of the halos makes a big difference in the masses.

Thus, the halos are very extended, a point that we will demonstrate more clearly later.

In summary, halo mass functions depend on how the halos are defined. Earlier workers (e.g., Efstathiou et al. 1988b; Carlberg & Couchman 1989) found good agreement between the Press-Schechter theory and simulations. However, the simulations were analyzed with a low-resolution group finder, FOF ($l = 0.2$), and the halos contained relatively few particles. Our results agree with this work, but show further that the Press-Schechter theory does not match well the CMF when higher resolution is used to identify halos made of thousands of particles. The disagreement is in the sense that the simulated halos are less massive than predicted. This occurs not because large halos have failed to collapse. Rather, merging does not immediately erase the substructure in large halos, contrary to the assumptions made in the Press-Schechter theory.

3. DISTRIBUTIONS OF HALOS: BACKGROUND

3.1. *The Schechter Luminosity Function*

We need to define physically motivated catalogs of halos in order to understand further the effects of dynamic range on halo formation and in order to compare the simulations with the observations. Total bound mass, as in the previous section, is only one way to characterize the halos. We can also ask how much mass is contained within a specified radius. This is equivalent to specifying $V_{\rm circ} = (GM/R)^{1/2}$. Empirically, $V_{\rm circ}$ is found to be nearly independent of R and to correlate well with optical luminosity. We will use these correlations—the Tully-Fisher (1977) relationship for spiral galaxies and the Faber-Jackson (1976) relationship for elliptical galaxies—to assign a luminosity to each halo.

Observations of spiral galaxies are measured in terms of their circular velocity and observations of elliptical galaxies are measured in terms of their average central radial velocity dispersion. (Technically, the elliptical observations are luminosity weighted measurements of radial velocities along the line of sight.)

We realize that we cannot adequately relate internal velocity dispersions of dark matter to velocity dispersions of centrally concentrated stars. Nevertheless, we define the quantities σ_1 and σ_r (σ_r is closer to what the observers measure) from the simulated galaxy halos as follows:

$$\sigma_1^2(R) = \frac{1}{3N_c}\sum_{i=1}^{N_c} |\boldsymbol{v}_i - \boldsymbol{v}_{\rm cm}|^2 ,$$
$$\sigma_r^2(R) = \frac{1}{N_c}\sum_{i=1}^{N_c} |(\boldsymbol{v}_i - \boldsymbol{v}_{\rm cm})\cdot \hat{\boldsymbol{r}}_i|^2 , \quad (3.1)$$

where N_c represents the number of bound particles within a distance R from the local density maximum and $\hat{\boldsymbol{r}}_i$ is the unit vector from the local density maximum to particle i. We do not attempt to distinguish the simulated halos as spirals or ellipticals; rather, we characterize all of the simulated halos in terms of their circular velocities.

Because the velocity dispersion tensor is radially anisotropic we find that σ_1 is typically $\sim$20% lower than σ_r. We study both quantities, using various cutoff radii (typically a few hundred kpc comoving), when comparing the velocity dispersions of massive simulated halos (perhaps associated with elliptical galaxies) with observations of the velocity dispersions of centrally concentrated stars. In order to test if either σ_1 or σ_r is a useful statistic, and because the stars are in orbits with smaller apapses than the dark matter, we use a crude, linear scaling law (derived from observations of M87) as discussed in greater detail in § 4.4.

For $\Omega = 1$ and $h = \frac{1}{2}$, the circular velocity, for an assumed spherical halo, as a function of total particle number in the simulation, N, and the comoving box size in Mpc, L, is

$$V_{\rm circ}(R) = 7.97 \text{ km s}^{-1}\sqrt{N_c(R)}\left(\frac{128^3}{N}\right)^{1/2} \times \left(\frac{L}{51.2 \text{ Mpc}}\right)^{3/2}\left(\frac{300 \text{ kpc}}{Ra/a_0}\right)^{1/2} , \quad (3.2)$$

where $N_c(R)$ is the total number of bound particles within a comoving distance R from the smoothed density maximum found by DENMAX. The present epoch is $a = a_0 \equiv \sigma_8$. In most of the figures, we assume that $a = a_0$ and we consider different possible normalizations by varying $\sigma_8 = a_0$. In one case below (Fig. 16), we fix a_0 and look at the evolution of halos for different a. In all cases, we take R to be a comoving radius (i.e., a proper radius at $a = a_0$) and we use the proper radius Ra/a_0 in the denominator. To get circular velocities measured at a fixed comoving radius, we set $a = a_0$.

In order to compute the observed distribution of galaxies as a function of $V_{\rm circ}$, i.e., $N(V_{\rm circ})\Delta V_{\rm circ}$, we assume a Schechter (1976) luminosity function with the form

$$\Phi(\mathscr{L})d\mathscr{L} = \Phi^* \exp(-\mathscr{L}/\mathscr{L}_*)(\mathscr{L}/\mathscr{L}_*)^\alpha d(\mathscr{L}/\mathscr{L}_*) , \quad (3.3)$$

where $\Phi(\mathscr{L})d\mathscr{L}$ is the density of galaxies in the luminosity range $\mathscr{L}$ to $\mathscr{L} + d\mathscr{L}$. We convert equation (3.3) into counts of halos in a (51.2 Mpc)^3 comoving volume as a standard reference for all of the simulations in bins of $V_{\rm circ}$ using a relationship for $\mathscr{L} = \mathscr{L}(V_{\rm circ})$. We also use blue magnitudes and selected values of Φ^* and $\mathscr{L}^*_{B_T}$ (both assuming $h = \frac{1}{2}$), and a value of α.

We define the distribution of halos, or number of halos binned by $V_{\rm circ}$, as

$$N(V_{\rm circ})\Delta V_{\rm circ} = \left(\frac{51.2 \text{ Mpc}}{L}\right)^3 \tilde{N}(V_{\rm circ})\Delta V_{\rm circ} , \quad (3.4)$$

where $\tilde{N}(V_{\rm circ})$ is the number of halos found in the simulation with circular velocities in the range $V_{\rm circ} \pm \Delta V_{\rm circ}/2$ with $\Delta V_{\rm circ} = 25$ km s^{-1}. The factor (51.2 Mpc/L)^3 is used to scale all of the results to comoving volumes (51.2 Mpc)^3 for comparison.

We compute the corresponding mean number of galaxies from the observations as follows, assuming $\mathscr{L}$ is related to M_{B_T} and $M_{B_T} = f(V_{\rm circ})$ for some function f given below:

$$N_{\rm Schechter}(V_{\rm circ})\Delta V_{\rm circ} = (51.2 \text{ Mpc})^3 \int_{x^{(1)}}^{x^{(2)}} \Phi(x)dx ,$$
$$M_{B_T}^{(1)} = f(V_{\rm circ} + \Delta V_{\rm circ}/2) ,$$
$$M_{B_T}^{(2)} = f(V_{\rm circ} - \Delta V_{\rm circ}/2) ,$$
$$\Phi[x(M_{B_T})] = \Phi^* x^\alpha \exp(-x) ; \quad x \equiv 10^{[M_{B(T)^*} - M_{B(T)}]/2.5} = \frac{\mathscr{L}}{\mathscr{L}^*} . \quad (3.5)$$

We use the central values of parameters found by Efstathiou, Ellis, & Peterson (1988a):

$$\Phi^* = (1.56 \pm 0.34) \times 10^{-2} h^3 \text{ Mpc}^{-3} ,$$
$$M^*_{B_T} = -19.68 \pm 0.10 - 2.5 \log_{10} h^{-2} ,$$

and

$$\alpha = -1.07 \pm 0.05 .$$

For the function $f(V_{\rm circ})$ for spiral galaxies we use the blue Tully-Fisher relation from Pierce & Tully (1988):

$$f_{\rm spiral}(V_{\rm circ}) \equiv M_{B_T} = -6.86 \log_{10} (2V_{\rm circ}) - 2.27 + 5 \log_{10} (50/85) + 0.569 . \quad (3.6)$$

The term $5 \log_{10} (50/85)$ is used to convert from a Hubble constant of 85 km s^{-1} Mpc^{-1} to 50 km s^{-1} Mpc^{-1}. The term 0.569 is used to correct for random inclinations following Tully & Fouque (1985).

For the function $f(V_{\rm circ})$ for elliptical galaxies we use the Faber-Jackson relation from our fit (unpublished) to elliptical data of Faber et al. (1989), assuming a Hubble constant of 50 km s^{-1} Mpc^{-1}:

$$f_{\rm elliptical}(V_{\rm circ}) \equiv M_{B_T} = -6.6364 \log_{10} (\sigma_1) - 5.884 , \quad (3.7)$$

where we relate σ_1 to $V_{\rm circ}$ using

$$\sigma_1 = F \frac{V_{\rm circ}}{\sqrt{3}} . \quad (3.8)$$

The factor F, discussed in the next section, is estimated from the simulations. This use of σ_1, however, is an oversimplification (mostly affecting high $V_{\rm circ}$) for reasons discussed earlier. Again, we reexamine the high-mass halos in detail in § 4.4, where we use σ_1, σ_r, and a linear scaling law derived from M87.

The final ingredient is to assume that 70% of the galaxies are spirals and 30% are ellipticals. This is also the assumption used by Frenk et al. (1988). In other words, we add together the results for spirals using equation (3.6) to relate circular velocities to absolute magnitudes and weighting equation (3.5) by 0.7 with the results for ellipticals using equation (3.7) to relate circular velocities to absolute magnitudes and weighting equation (3.5) by 0.3. Dressler (1980), however, found a higher concentration of ellipticals in rich clusters compared with lower density regions. Postman & Geller (1984) found for the CfA survey that (1) the relative numbers of galaxies are 65% spirals, 23% S0's, and 12% ellipticals and (2) there is a dramatic increase in the relative number of spirals in the field compred with dense regions. These percentages can alter the estimates at the high-mass end.

3.2. σ_1 *versus* $V_{\rm circ}$

The factor F in equation (3.8) is measured empirically from the simulation CDM 16(144^3, 100, 85) using DENMAX halos analyzed with a 512^3 grid. White et al. (1987) used $F = 1$ (in our notation) but the same authors used $F = 1.1$ in Frenk et al. (1988).

Because the Plummer softening in CDM 16 is $\epsilon = 65$ kpc comoving (or $R_{1/2} = 85$ kpc) we cannot directly determine $\sigma_1(R)$ or $V_{\rm circ}(R)$ at the distance where optical observations of real galaxies are made. Optical observations of central velocity dispersions of large elliptical galaxies are made on scales of a few kpc to ~6 kpc (see Franx, Illingworth, & Heckman 1989). Optical observations of circular velocities of large spiral galaxies are made out to ~10 kpc. Rubin et al. (1985) studied 16 large spiral galaxies where they could measure velocities out to large radii. The average maximum distance for which they made measurements was 16.4 kpc and the maximum distance for the 16 galaxies was 51.2 kpc. We consider the limitations arising from our measurements at large radii as we proceed.

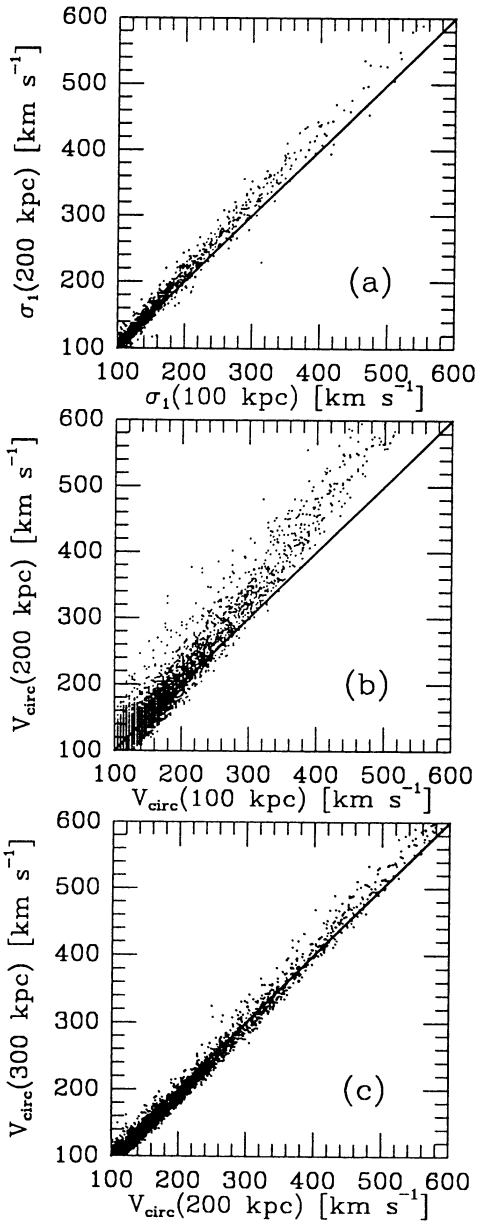

FIG. 9.—σ_1 and $V_{\rm circ} \equiv (GM/R)^{1/2}$ from CDM 16(144^3, 100, 85) at $\sigma_8 = 0.7$. Each point represents one halo. We show various comoving cuts. (*a*) σ_1(200 kpc) vs. σ_1(100 kpc). (*b*) $V_{\rm circ}$(200 kpc) vs. $V_{\rm circ}$(100 kpc). (*c*) $V_{\rm circ}$(300 kpc) vs. $V_{\rm circ}$(200 kpc).

What is a value of R for computing σ_1 where the results are independent of R? In Figure 9 (*top panel*) we show σ_1 evaluated using $R = 100$ kpc comoving versus $R = 200$ kpc comoving. The slight increase in σ_1 for $R = 200$ kpc comoving versus $R = 100$ kpc comoving (*top panel*) indicates that contributions from particles at large separations are still important for the most massive halos. We find this trend to be larger when comparing results from $R = 50$ kpc comoving versus $R = 100$ kpc comoving, indicating that $R = 100$ kpc comoving is too small. We find this trend to be small when comparing results from $R = 200$ kpc comoving versus $R = 300$ kpc comoving, indicating that $R = 200$ kpc comoving is adequate. We find similar results at $\sigma_8 = 0.7$ and $\sigma_8 = 1.0$.

What is a value of R for computing V_{circ} where the results are independent of R? In Figure 9 we also show computations for V_{circ} using $R = 100$ kpc comoving, 200 kpc comoving, and 300 kpc comoving. The results indicate that $R = 200$ kpc comoving is acceptable (*bottom panel*) while $R = 100$ kpc comoving again is too small (*middle panel*).

What is an empirical value of F in equation (3.8)? In Figure 10 we show V_{circ}/σ_1 versus V_{circ} (all computed with $R = 200$ kpc comoving) at $\sigma_8 = 0.5$, 0.7, and 1.0 for halos from CDM 16(144^3, 100, 85). The solid lines indicate $F = 1$ (i.e., $V_{circ}/\sigma_1 = 3^{1/2}$) and the dotted lines indicate $F = 1.1$ (i.e., $V_{circ}/\sigma_1 = 3^{1/2}/11$). There is less scatter for high values of V_{circ} versus low values of V_{circ}. The factor F affects the conversion of V_{circ} to σ_1 for ellipticals. Ellipticals dominate at the high mass end where, at $\sigma_8 = 0.5$, $F = 1.1$ works slightly better than $F = 1$. However, when we show the observed number of halos in § 4 we use both $F = 1$ and $F = 1.1$—the latter yields fewer bright halos since it effectively raises σ_1 for a given V_{circ} implying a brighter elliptical galaxy (or equivalently, $F = 1.1$ effectively assigns a smaller stellar velocity dispersion for a given σ_1).

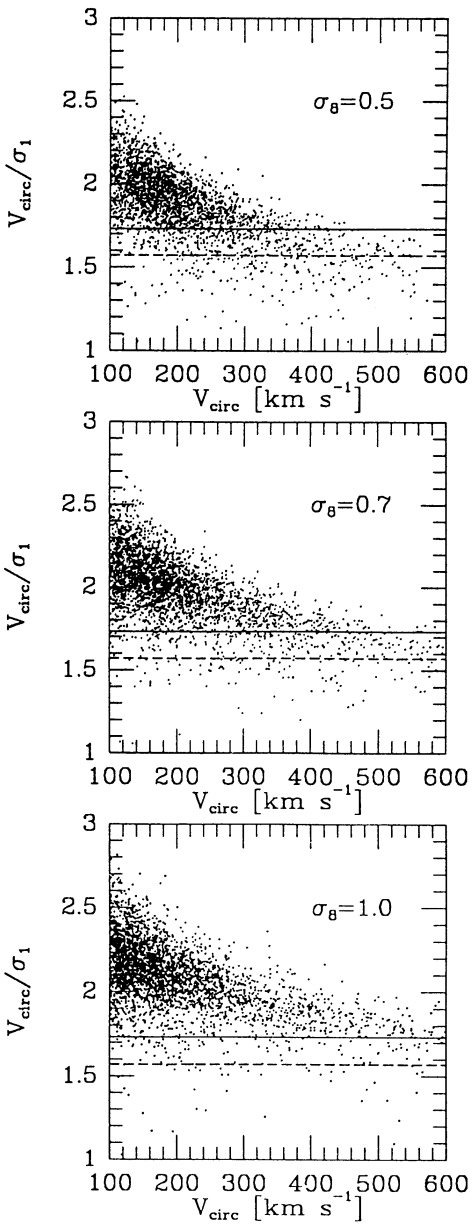

FIG. 10.—V_{circ}/σ_1 vs. V_{circ} (all computed using $R = 200$ kpc comoving) from CDM 16(144^3, 100, 85). Solid lines are for $V_{circ}/\sigma_1 = 3^{1/2}$, or $F = 1$ in eq. (3.8), and dashed lines are for $V_{circ}/\sigma_1 = 3^{1/2}/1.1$, or $F = 1.1$ in eq. (3.8).

In summary, we compute the number of halos scaled to (51.2 Mpc)^3 comoving volumes assuming a Schechter luminosity function ($\Phi^* = 1.56 \times 10^{-2} h^3$ Mpc^{-3} and $M^*_{B_T} = -19.68 - 2.5 \log_{10} h^{-2}$ with $h = \frac{1}{2}$ and $\alpha = -1.07$). We assume 70% of the galaxies are spirals with a Tully-Fisher relation given by equation (3.6) and 30% of the galaxies are ellipticals with a Faber-Jackson relation given by equation (3.7). We convert elliptical measurements in terms of σ_1 to V_{circ} using equation (3.8) for both $F = 1$ and $F = 1.1$. For the massive halos $F = 1$ is adequate except at $\sigma_8 = 0.5$ where $F = 1.1$ is slightly better.

3.3. *Circular Velocity Profiles*

We now examine circular velocity profiles and one-dimensional velocity dispersion profiles from CDM 12(64^3, 51.2, 52) in Figure 11. We extract several facts from these plots. First, the circular velocities are very flat for nearly all the halos, except for a few massive ones, for $R \gtrsim 150$ kpc comoving. We also see that the circular velocities are flat for many of the midsize halos down to about 80 kpc comoving (twice the Plummer softening length). We conclude that 150 kpc comoving is a good place to characterize the circular velocities for this simulation at all epochs. We are making a significant error only for a handful of the most massive halos. The rising circular velocities for the most massive halos are not an artifact of softening (see § 4.4).

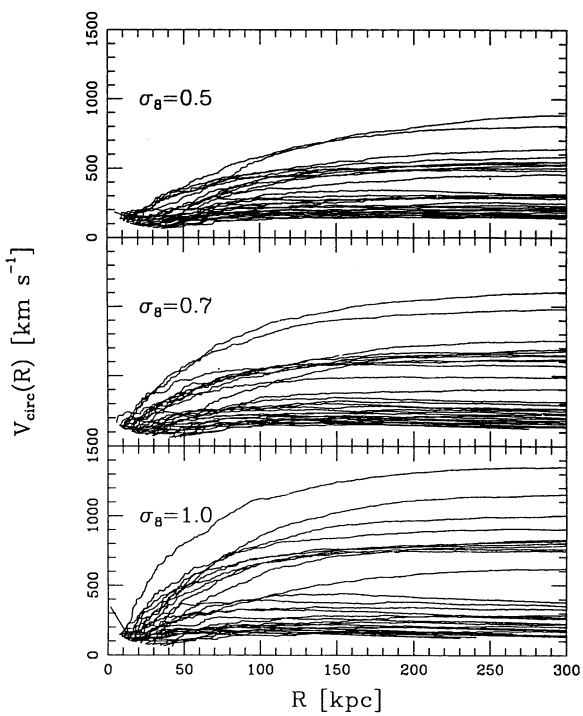

FIG. 11.—Circular velocity profiles for 512^3 DENMAX halos from CDM 12(64^3, 51.2, 52; $\epsilon = 40$ kpc comoving). For each halo we computed V_{circ} at 150 kpc comoving: V_{150}. We then sorted the halos from large to small V_{150}. We show the top 10 halos and then every 20th halo thereafter, all the way down to $V_{150} = 150$ km s^{-1}. (This procedure is done independently at each epoch.)

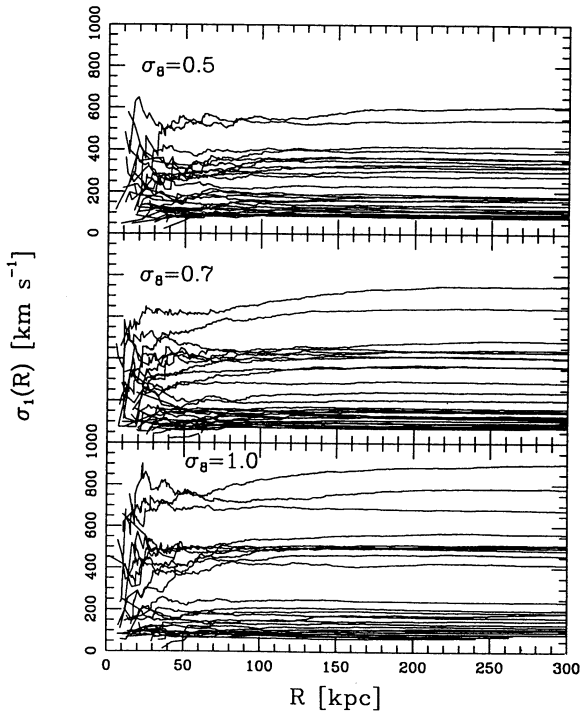

FIG. 12.—Cumulative velocity dispersion profiles $\sigma_1(R)$ for the same halos shown in Fig. 11.

We also study CDM 1 ($R_{1/2} = 280$ kpc comoving) and CDM 16 ($R_{1/2} = 85$ kpc comoving) and we find that $R = 300$ kpc comoving is suitable for CDM 1 and $R = 200$ kpc comoving is suitable for CDM 16. In most cases, we use $R = 150$ kpc comoving for the $R_{1/2} = 52$ kpc comoving simulation; $R = 200$ kpc comoving for the $R_{1/2} = 85$ kpc comoving simulation; and $R = 300$ kpc comoving for the $R_{1/2} = 280$ kpc comoving simulation. These values are chosen where $V_{\rm circ}$ is flat for nearly all of the halos.

We compare our circular velocity profiles to simulations by others with much higher force resolution. The $\Omega = 1$ CDM simulations of Dubinski & Carlberg (1991) used 33,000 particles in a 2.3 Mpc radius sphere. The typical particle mass is $1.2 \times 10^8\ M_\odot$ and the Plummer softening is 1.4 kpc. In their Figure 4 they show several circular velocity profiles with halos that have maximum circular velocities of about 290 km s^{-1}. These halos have flat circular velocities between about 10 kpc and 60 kpc (there is a very slight decrease over this range). The circular velocities rise on a scale a few times the Plummer softening length as we also find in our simulations.

The simulations of Warren et al. (1991) used roughly a million particles in a 5 Mpc radius sphere and a Plummer softening of 5 kpc. For circular velocity profiles that have maximum circular velocities of about 150 km s^{-1} they found that the profiles are rising out to a distance of about 30 kpc—again, several Plummer lengths. They also found that their profiles are falling typically beyond a distance of about 40 kpc. In our P^{3}M simulations we do not find falling circular velocity profiles until a distance of about 100 kpc. One reason for this discrepancy is that Warren et al. did not use a CDM power spectrum—rather, they used $P(k) \propto k$ on large scales with a shrp transition, at 1.5 Mpc, to $P(k) \propto k^{-2}$ on small scales. The behavior of circular velocities is a function of the effective index in the initial power spectrum (Hoffman & Shaham 1985).

We assume that if we had used force softening below the typical ~ 10 kpc observed scale, as in the simulations of Dubinski & Carlberg (1991) and Warren et al. (1991), that our circular velocity profiles might remain flat down to these scales. Therefore, we do not expect to make a significant error by estimating $V_{\rm circ}$ using $R \gtrsim 150$ kpc comoving. We cannot use circular velocities to characterize the most massive halos because observational data for massive halos are based on velocity dispersions, not circular velocities. We explore the properties of σ_1 below.

There is cause for concern when using simulations with force softening far beyond a few kpc—the scale beyond which most spiral galaxies are observed to have flat rotation curves. Are we able to adequately resolve individual halos? We comment on several issues related to this question. (1) Using $\sim(1/\Phi^*)^{1/3}$, and $\Phi^* = 1.95 \times 10^{-3}$ Mpc^{-3}, we find the mean spacing between bright galaxies is ~ 8 Mpc. This is much greater than our fiducial radius ~ 200 kpc. Observations show flat rotation curves "as far as the eye can see" for most spiral galaxies (Rubin et al. 1985). It is therefore possible that real galaxies have flat rotation curves beyond 200 kpc. (2) The mean galaxy spacing is much smaller in rich clusters. It is possible that some of our massive halos are mergers where dissipative effects might allow many galaxies to survive in a single halo (White & Rees 1978; Katz & White 1993). In Paper II we break up these systems using various methods in an attempt to estimate the effects on clustering. In this paper, however, we consider the massive halos at face value and we examine the implications for CDM in § 4.3. We compare results from the $\epsilon = 40$ kpc comoving simulation with results from the $\epsilon = 65$ kpc comoving simulation and we ask if the distributions of halos are significantly different.

Last, we show $\sigma_1(R)$ for the $\epsilon = 40$ kpc comoving simulation CDM 12(64^3, 51.2, 52) in Figure 12. (These are the same halos shown in Fig. 11.) The first thing we notice is that the profiles are very flat down to about 40 kpc comoving, the Plummer softening scale. (On smaller scales we are limited by both force and mass resolution.) Also, the profiles for the most massive halos are flat down to typically 100 kpc comoving. In § 4.4 we use σ_r computed at large radii (similar to σ_1) to compare simulated halos with the observations.

4. DISTRIBUTIONS OF SIMULATED HALOS

4.1. *Overview*

We now study the distributions of simulated halos as a function of $V_{\rm circ}$. The results of the computations of $N(V_{\rm circ})\Delta V_{\rm circ}$ scaled to (51.2 Mpc)^3 comoving volumes are presented in Figures 13 through 16. We include observational estimates using both $F = 1$ and $F = 1.1$ to relate σ_1 to $V_{\rm circ}$ for comparison.

We focus our efforts on the following three simulations: CDM 1(128^3, 51.2, 280), CDM 12(64^3, 51.2, 52), and CDM 16(144^3, 100, 85). CDM 1 offers good mass resolution ($m_{\rm part} = 4.4 \times 10^9\ M_\odot$), CDM 12 offers good force resolution (Plummer softening of 40 kpc comoving), and CDM 16 offers fairly good mass and force resolution ($m_{\rm part} = 2.3 \times 10^{10}\ M_\odot$; Plummer softening of 65 kpc comoving), yet is computed in a 100 Mpc box. Again, we demonstrated in § 2 that the CMF is not very sensitive to the box size but we demonstrate in Paper II that clustering statistics require boxes larger than 51.2 Mpc on a side.

Our goal in the following sections is to attempt to constrain the amplitude of the primeval density fluctuations of the $\Omega = 1$

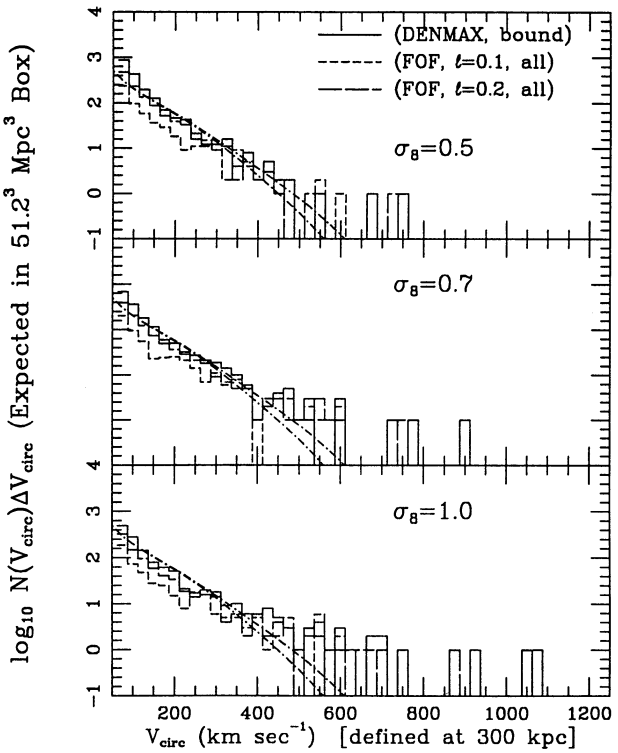

FIG. 13.—Distribution function of circular velocity for CDM 1(128³, 51.2, 280) with the circular velocities measured at 300 kpc comoving. The results are scaled to a comoving volume of (51.2 Mpc)³ in all of the distribution plots (Figs. 13 through 16) for comparison. The dot-dashed curves in these plots are for a Schechter function ($F = 1$ and $F = 1.1$; the latter gives slightly fewer numbers for bright elliptical halos). We use 512³ DENMAX (*solid histograms*), FOF ($l = 0.1$, *short-dashed histograms*), and FOF ($l = 0.2$, *long-dashed histograms*). The histograms, high to low values at $V_{circ} \sim 200$ km s^{-1}, are for DENMAX, then FOF ($l = 0.2$), then FOF ($l = 0.1$). For $\sigma_8 = 1$, each method found two halos for $V_{circ} \geq 800$ km s^{-1}. The bins at $V_{circ} = 875$ km s^{-1} and 1050 km s^{-1} each contain one FOF ($l = 0.1$) halo and one FOF ($l = 0.2$) halo. The bins at $V_{circ} = 925$ km s^{-1} and 1075 km s^{-1} each contain one DENMAX halo.

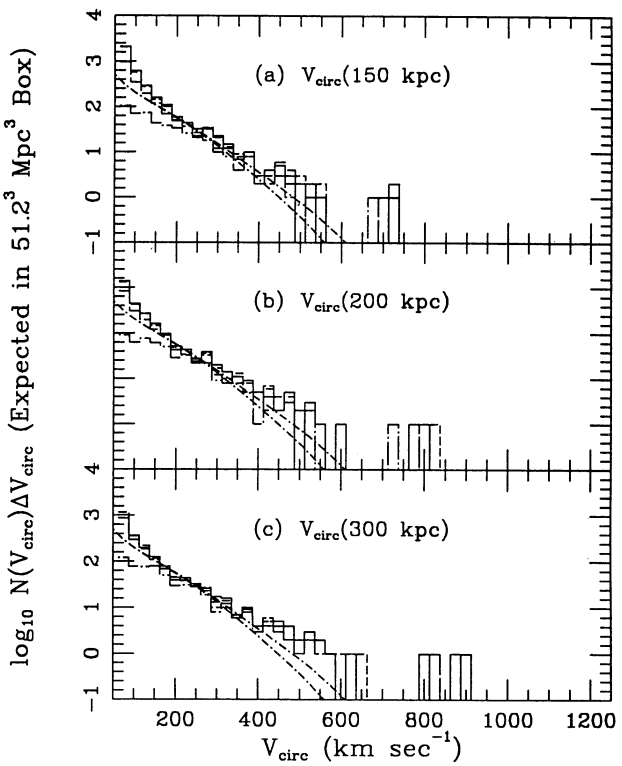

FIG. 14.—Distribution function of circular velocity for CDM 12(64³, 51.2, 52) analyzed at $\sigma_8 = 0.5$ with DENMAX grids of 512³ (*solid histograms*), 256³ (*short-dashed histograms*), 128³ (*long-dashed histograms*), and 64³ (*dot-dashed histograms*). The comoving radii used to define the circular velocities are (*a*) 150 kpc, (*b*) 200 kpc, and (*c*) 300 kpc. The 512³, 256³, and 128³ DENMAX grids are nearly indistinguishable except for large V_{circ}. The cores 64³ DENMAX grid fails to match up to the other histograms. In the bottom panel, each grid identified two halos above 700 km s^{-1}. The 800 km s^{-1} bin contains a 64³ grid halo and a 512³ grid halo. The 825 km s^{-1} bin contains a 128³ grid halo and a 256³ grid halo. The 875 km s^{-1} bin contains a 512³ grid halo. The 900 km s^{-1} bin contains a 64³ grid halo, a 128³ grid halo, and a 256³ grid halo.

CDM model from halo circular velocity distributions. We devote separate subsections for both high-mass and low-mass halos, which require special treatment for determining reliable simulated and observed distributions.

4.2. *Circular Velocity Distributions of Simulated Halos*

We measure $N(V_{circ})\Delta V_{circ}$ from the simulations. We ask the questions: (1) Over which range of circular velocities do the results agree with the observations? (2) Over which range of circular velocities do the results disagree with the observations? (3) Do the results depend on numerical resolution and techniques for identifying halos?

In Figure 13 we show $N(V_{circ})\Delta V_{circ}$ at $\sigma_8 = 0.5$, 0.7, and 1.0 for an analysis of CDM 1(128³, 51.2, 280) using 512³ DENMAX and FOF($l = 0.1$) and FOF($l = 0.2$). We see from Figure 13 that the number of halos agrees with the observations very well from about 150 km s^{-1} to 350 km s^{-1} for DENMAX and FOF($l = 0.2$). The results for FOF($l = 0.1$) do not fare as well. These statements are true for all three epochs; however, the excess number of massive halos gets worse with increasing σ_8. DENMAX is a compromise between FOF ($l = 0.2$) which sometimes merges halos and FOF($l = 0.1$) which fails to produce some halos. These results are encouraging for studies that use FOF($l = 0.2$) such as Frenk et al. (1988); however, FOF($l = 0.2$) occasionally links together visually distinct halos.

We now study the effects of force resolution, choice of DENMAX grid, and choice of R (used to compute V_{circ}) on $N(V_{circ})\Delta V_{circ}$. We show $N(V_{circ})\Delta V_{circ}$ at $\sigma_8 = 0.5$ for CDM 12(64³, 51.2, 52) in Figure 14. The first thing we notice is that the agreement with the number of simulated halos with the observations from 150 km s^{-1} to 350 km s^{-1} is even better than it is for the low force resolution PM simulation discussed above, particularly for $V_{circ} \sim 200$ km s^{-1}. We also see that the results are not very sensitive to the choice of R except for the few very massive halos. This is not surprising since most of the circular velocity profiles are flat beyond 150 kpc comoving except for the most massive halos—cf. Figure 11.

It is encouraging that the results are not very sensitive to the choice of DENMAX grid except for the most massive halos and for the 64³ grid. This is not true for the halo masses described by the CMF in § 2—we show later that this is because the different DENMAX grids significantly affect peripheral particles beyond the distance R used to compute the circular velocities. It is not surprising that the very coarse 64³ grid fails to match up to the finer grids.

We conclude this discussion by testing the sensitivity of the agreement of the number of simulated halos with the observa-

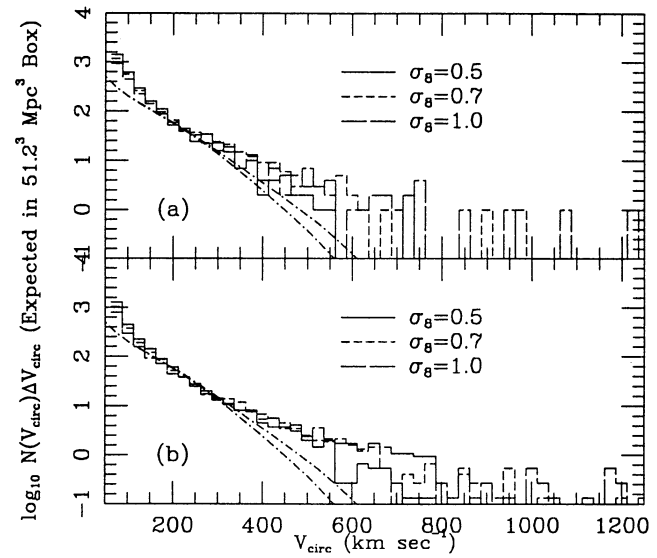

FIG. 15.—Distribution function of circular velocity for 512^3 DENMAX halos from (*a*) CDM 12(64^3, 51.2, 52) and from (*b*) CDM 16(144^3, 100, 85). We use a 150 kpc comoving distance to compute V_{circ} for CDM 12 and a 200 kpc comoving distance to compute V_{circ} for CDM 16. The results are shown at $\sigma_8 = 0.5$ (*solid histogram*), 0.7 (*short-dashed histograms*), and 1.0 (*long-dashed histograms*); they overlap except for high V_{circ} where there are more halos for larger values of σ_8.

tions for the different P^{3}M simulations (Fig. 15) and then by studying the evolution of the number of the simulated halos (Fig. 16).

In Figure 15 we show $N(V_{circ})\Delta V_{circ}$ for CDM 12(64^3, 51.2, 52; $\epsilon = 40$ kpc comoving) (*top panel*) and for CDM 16(144^3, 100, 85; $\epsilon = 65$ kpc comoving) (*bottom panel*), both analyzed with a 512^3 DENMAX grid. We extract several facts from Figure 15. First, the trend of increasing number of halos with increasing force resolution is verified comparing the simulations with $\epsilon = 40$ kpc comoving (*top panel*) and $\epsilon = 65$ kpc comoving (*bottom panel*), but the differences are small. We found in § 2 that the CMF was higher for higher mass resolution simulations and for higher force resolution simulations independently; but here force resolution must be dominating because the $\epsilon = 40$ kpc comoving simulation has slightly lower mass resolution than the $\epsilon = 65$ kpc comoving simulation, yet still produces slightly more halos at a given V_{circ}. We also found in § 2 that the differences in the CMF versus mass resolution were much smaller when we imposed a radius cut on the masses. This is equivalent to computing circular velocities.

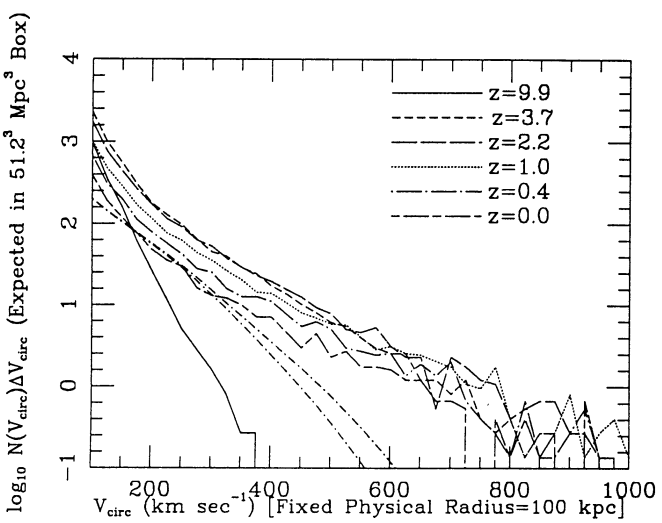

FIG. 16.—Same as Fig. 15*b*, except that we use a fixed physical radius of 100 kpc to compute circular velocities of halos in a $(51.2\ \mathrm{Mpc})^3$ comoving volume. The epochs are listed in terms of the redshift $z = 1/a - 1$ where we take $a_0 = \sigma_8 = 1$ to be the present day. This plot depicts evolution.

In Figure 16 we show V_{circ} for CDM 16(144^3, 100, 85) using a fixed physical radius. We list the epochs as redshifts, $z = 1/a - 1$, because here we are studying the evolution of the halos for a fixed normalization. We assume that the present epoch, $z = 0$, is $a_0 = \sigma_8 = 1$. We keep the physical radius cut constant at 100 kpc by using a $100a_0/a$ kpc comoving radius cut in equation (3.2). The vertical axis is scaled to a $(51.2\ \mathrm{Mpc})^3$ comoving box, however.

We see in the panels of Figure 16 that $N(V_{circ})\Delta V_{circ}$ (using a fixed proper radius) evolves strongly with redshift. At $z = 9.9$ halos are still forming. The major era when galaxies begin to take on the observed distribution is around $z = 3.7$–2.2. Further evolution indicates that the halos are merging, i.e., the curves are decreasing. At intermediate circular velocities ($V_{circ} = 200$ km s^{-1}), the number of halos decreases by a factor of 3.7 from the maximum at $z \sim 3.7$ to $z = 0$. For smaller halos ($V_{circ} = 150$ km s^{-1}) the effect is higher, a factor of 4.7 from the maximum at $z \sim 3.7$ to $z = 0$. From $z = 0.4$ to $z = 0$ the factor is roughly constant at ~ 1.5 over wide range of V_{circ}. The most massive halos grow at the expense of the smaller ones. For halos with total bound masses exceeding $2.3 \times 10^{13}\ M_\odot$ in CDM 16(144^3, 100, 85) (i.e., 1000 particles), we find 245 halos at $z = 1$, 292 at $z = 0.4$, and 285 at $z = 0$. Therefore, the number of massive halos, unlike the lower mass halos, grows little for $z < 1$.

The mergers implied by Figure 16 are interesting in themselves, and they are important for Paper II where merging forms massive systems which have a profound effect on galaxy clustering and velocity statistics. Frenk et al. (1988) also found merging in their simulations with decreasing redshift. There exists some observational evidence for merging. Excess counts of faint galaxies (Tyson 1988) compared with present galaxy populations suggest the possibility of merging (Guiderdoni & Rocca-Volmerange 1990; Cowie, Songaila, & Hu 1991). The merger hypothesis is not without controversy, however, for other possibilities and complications, highlighted by various authors, include (1) luminosities may evolve more rapidly for faint galaxies than for bright galaxies (e.g., Broadhurst, Ellis, & Shanks 1988); (2) the geometry of the universe may be different from Einstein–de Sitter (e.g., Fukugita et al. 1990); or (3) the faint galaxies may represent a separate population (e.g., Efstathiou et al. 1991).

Cowie et al. (1991) argue that the faint galaxy excess is a factor $\sim$4–5 from $z \sim 0.25$ to $z = 0$ assuming no luminosity evolution for these modest redshifts. Although CDM 16 predicts only a factor of ~ 1.5 from $z = 0.4$ to $z = 0$, we cannot accurately address galaxy merging with our dark simulations for the following reasons: (1) we *underestimate* merging by always associating one galaxy per halo and (2) we *overestimate* merging by always assuming that when halos merge their associated galaxies merge. Complications aside, since the reduction is ~ 1.5 over a wide range in V_{circ}, we may naively assume that only $\sim(1\text{–}1/1.5) \times 0.7 = 23\%$ of the spirals (assuming a 70% spiral fraction) have not experienced a major

TABLE 2

V_{circ} FOR MASSIVE HALOS FROM CDM 12(64^3, 51.2, 52) AT $\sigma_8 = 0.5$

DENMAX GRID	HALO	$R \le 150$ kpc Rank	$R \le 150$ kpc V_c (km s^{-1})	$R \le 200$ kpc Rank	$R \le 200$ kpc V_c (km s^{-1})	$R \le 300$ kpc Rank	$R \le 300$ kpc V_c (km s^{-1})	$R < \infty$ Rank	$R < \infty$ Mass ($M_\odot$)
512^3	A	1	738	1	807	1	891	1	1.5×10^{14}
512^3	B	2	712	2	774	2	811	2	1.0×10^{14}
512^3	C	3	545	3	590	3	630	3	6.2×10^{13}
512^3	D	4	528	4	552	4	528	4	4.9×10^{13}
256^3	A	1	737	1	814	1	897	1	2.6×10^{14}
256^3	B	2	720	2	778	2	820	2	1.6×10^{14}
256^3	C	3	546	3	597	3	641	3	9.6×10^{13}
256^3	D	4	536	4	554	4	589	4	6.6×10^{13}
128^3	A	1	718	1	807	1	899	1	4.3×10^{14}
128^3	B	2	710	2	773	2	818	2	1.9×10^{14}
128^3	C	3	542	3	597	3	636	3	1.4×10^{14}
128^3	D	4	528	4	558	4	583	4	1.2×10^{14}
064^3	A	1	706	1	803	1	892	1	4.6×10^{14}
064^3	B	2	660	2	732	2	805	2	2.2×10^{14}
064^3	C	3	482	3	535	3	605	3	1.7×10^{14}
064^3	D	9	437	5	499	4	575	4	1.3×10^{14}

merger since $z \sim 0.4$. This is problematic since Toth & Ostriker (1992) argue that high merger rates in the last 5 Gyr ($z = 0.37$ for $\Omega = 1$, $H_0 = 50$ km s^{-1} Mpc^{-1}) can heat disk galaxies beyond observed levels. Furthermore, if we were to identify $a_0 = \sigma_8 = 0.5$ as the present day, Figure 16 would still apply if the V_{circ} values were all multiplied by $2^{-1/2}$. This would move the $\sigma_8 = 0.5$ curve ($z = 1.0$ in the figure) into agreement with the Schechter function, as it should from Figure 15. From this we conclude that in the CDM model merging should continue into the future at a rate as prodigious as the recent past, further violating the Toth & Ostriker (1992) limits. For a more detailed examination of merging in CDM models, see Kauffmann & White (1993).

4.3. *Massive Halos: Computational Issues*

Since the number of halos from CDM 16(144^3, 100, 85) agrees with the observed number of halos in the range 160 km s^{-1} $\lesssim V_{circ} \lesssim$ 350 km s^{-1} we now focus on the discrepancies outside these ranges. In this section we explore circular velocities at various radii and we investigate the sensitivity of the formation of massive halos to dynamic range and to methods for identifying the halos. In § 4.4 we compare the number of simulated halos with high σ_r to the number of observed bright ellipticals, followed by a discussion of low-mass halos in § 4.5. The purpose of *this* section is to reveal which computational effects, and why, affect the massive halos.

We present the four most massive halos at $\sigma_8 = 0.5$ from CDM 12(64^3, 51.2, 52) in Table 2 and from CDM 1(128^3, 51.2, 280) in Table 3. The halos are labeled A, B, C, and D. These two simulations use equivalent initial conditions. Corresponding halos are identified. In the tables we list the circular velocities in km s^{-1} using $R = 150$ kpc comoving, 200 kpc comoving, and 300 kpc comoving. We also list the bound masses ($R < \infty$) in solar masses. In Table 2 the results are tabulated for a 512^3, 256^3, 128^3, and 64^3 DENMAX grid, all at $\sigma_8 = 0.5$. In each column we also list a local rank. The number

TABLE 3

V_{circ} FOR MASSIVE HALOS FROM CDM 1(128^3, 51.2, 280) AT $\sigma_8 = 0.5$

METHOD	HALO	$R \le 150$ kpc Rank	$R \le 150$ kpc V_c (km s^{-1})	$R \le 200$ kpc Rank	$R \le 200$ kpc V_c (km s^{-1})	$R \le 300$ kpc Rank	$R \le 300$ kpc V_c (km s^{-1})	$R < \infty$ Rank	$R < \infty$ Mass ($M_\odot$)
512^3 DENMAX	A	1	543	1	631	1	748	1	1.3×10^{14}
512^3 DENMAX	B	2	508	2	586	2	678	2	1.2×10^{14}
512^3 DENMAX	C	3	419	3	481	3	555	3	7.7×10^{13}
512^3 DENMAX	D	8	342	7	391	9	426	9	3.1×10^{13}
256^3 DENMAX	A	1	541	1	634	1	756	1	1.9×10^{14}
256^3 DENMAX	B	2	507	2	592	2	684	2	1.5×10^{14}
256^3 DENMAX	C	3	419	3	482	3	564	3	1.1×10^{14}
256^3 DENMAX	D	8	343	5	416	4	549	4	1.0×10^{14}
FOF ($b = 0.1$)	A	1	487	1	594	1	738	1	1.9×10^{14}
FOF ($b = 0.1$)	B	2	375	2	465	2	599	2	1.0×10^{14}
FOF ($b = 0.1$)	C	10	312	4	411	4	539	3	6.8×10^{13}
FOF ($b = 0.1$)	D	4	342	3	415	3	545	4	5.2×10^{13}
FOF ($b = 0.2$)	A	1	475	1	591	1	735	1	3.7×10^{14}
FOF ($b = 0.2$)	B	70	178	52	221	29	311	2	1.9×10^{14}
FOF ($b = 0.2$)	C	6	297	4	383	3	531	3	1.2×10^{14}
FOF ($b = 0.2$)	D	2	332	2	410	2	551	4	8.4×10^{13}

n means the halo is the nth largest halo in the catalog using the method for halo identification mentioned in the first column. Note that the circular velocity profiles for these massive halos are still rising far beyond the softening scale. Here we are interested in their profiles at large radii. We use σ_r and V_{circ} extrapolated to more reasonable radii in the next section.

We use Table 2 to study the effect of the choice of R and the DENMAX grid on the massive halos. The first important feature brought out is that V_{circ} increases with increasing radii. These massive halos have extended halos with rising circular velocities at these scales (cf. Fig. 11). The next trend we observe is that the circular velocities, unlike the CMF without a radius cut, are not very sensitive to the choice of DENMAX grid. However, the slight differences are explained below.

In Figure 17 the bound particles from halo B found in CDM 12(64^3, 51.2, 52) are shown using the various DENMAX grids. We see that the coarser DENMAX grids ($\leq 256^3$) merge the massive halo with an additional small halo (located at $x \approx 200$ kpc comoving, $y \approx -200$ kpc comoving). The mass of this "appendage" is small and is far enough away from the core (about 300 kpc comoving) so that it contributes little to the circular velocity defined within 300 kpc comoving. Nevertheless, it reveals substructure present in the higher force resolution simulation.

The lower resolution DENMAX grids also lead to the inclusion of more peripheral (distant) particles. This is not serious since this does not involve a lot of mass and involves only particles well beyond 300 kpc comoving from the halo core. When the DENMAX grid is finer than the interparticle separation in the periphery, the density gradients are not present to move the particles into the halo. This fact partially explains why the CMF (in § 2), based on total bound masses, is more sensitive than V_{circ} to variations of the DENMAX grid.

We now consider the effects of force resolution. In Figure 18 we show the same halo B but from the low force resolution PM simulation CDM 1(128^3, 51.2, 280)—we show every eighth particle for comparison with the 64^3 particle P^{3}M simulation.

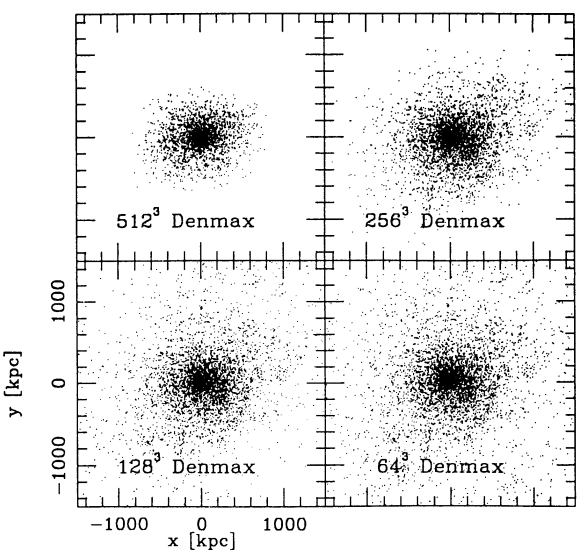

FIG. 17.—The bound particles of halo B (see Table 2) from CDM 12(64^3, 51.2, 52) at $\sigma_8 = 0.5$ are shown as found by the various DENMAX analyses. The images are shown as $x - y$ projections in units of comoving kpc. The 512^3 DENMAX analysis is able to resolve the small halo present in the other panels (located at $x \approx 200$ kpc and $y \approx -200$ kpc).

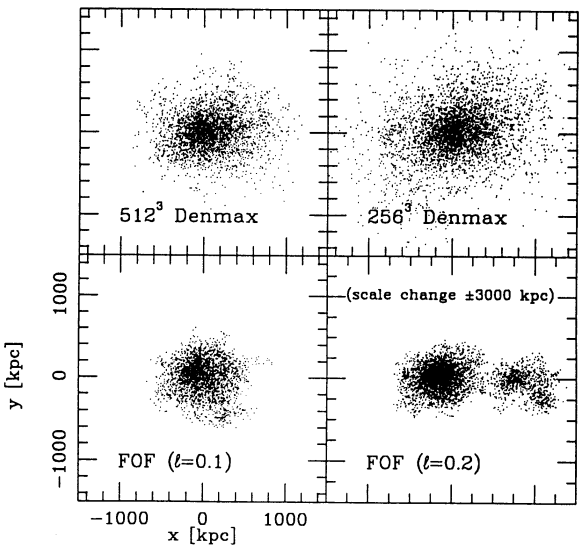

FIG. 18.—The bound particles of halo B (see Table 3) from CDM 1(128^3, 51.2, 280) at $\sigma_8 = 0.5$ found by the 256^3 and 512^3 DENMAX analyses and by the FOF($l = 0.1$) and FOF($l = 0.2$) analyses. (For FOF we do not remove the unbound particles.) We show every eighth particle to facilitate a comparison with the 64^3 particle simulation shown in Fig. 17. There is not much difference in the two DENMAX analyses (apart from the peripheral particles) because the PM forces are computed on a 256^3 grid. The FOF($l = 0.2$) analysis reveals a dramatic shortcoming of FOF—namely the linking together of several dynamically distinct halos.

The force resolution is too low to produce the "appendage" that we see in the P^{3}M simulation—therefore, there is no significant difference between the 512^3 grid DENMAX and the 256^3 grid DENMAX results. We conclude that high force resolution reveals more substructure than low force resolution and that high-resolution DENMAX grids are required to reveal this substructure.

We see in the lower right panel of Figure 18 a major failing of FOF($l = 0.2$). This is a particularly pathological example. Of course, we could naturally prune this halo into separate halos. It is not practical, however, to examine visually and prune manually the thousands of halos produced in each simulation.

The CDM 1 PM halos A–D, corresponding to the halos studied in the CDM 12 P^{3}M simulation, are tabulated in Table 3. The results are shown for two DENMAX grids and two FOF linking parameters, all at $\sigma_8 = 0.5$. From Table 3 we conclude: (1) The 512^3 DENMAX results compare well with the 256^3 DENMAX results. (2) The FOF analyses fail to agree with the DENMAX analyses. The difference between FOF ($l = 0.1$) and FOF($l = 0.2$) is not too great since these massive PM halos do not have a lot of substructure. The exception is halo B in the FOF($l = 0.2$) analysis. This is the pathological halo shown in the lower right panel of Figure 18. Three visually distinct halos are merged together and the center of mass is such that the "halo" is highly nonspherical, leading to unreliable circular velocities.

We also find, from Table 3, that the P^{3}M halos are more compact than the PM halos. If we compare V_{circ} defined at 150 kpc comoving in Table 2 for P^{3}M CDM 12 with V_{circ} defined at 300 kpc comoving in Table 3 for PM CDM 1, we find comparable values of V_{circ}. By the time we got out to 300 kpc comoving in the PM simulation we pick up enough particles to give the same circular velocity as the P^{3}M simulation using 150 kpc comoving. This is because we choose values of R to be

the radius where most of the circular velocities are flat. These radii are directly related to the force resolution. However, things do not always work out this nicely for the massive halos that have rising circular velocity profiles, as we can see by comparing halo D in Table 2 for P^{3}M CDM 12 using 150 kpc comoving and halo D in Table 3 for PM CDM 1 using 300 kpc comoving. The differences in circular velocities are significant enough to shift some of the massive halos into adjacent 25 km s^{-1} bins.

We now summarize some effects arising from the computational techniques that influence the number of massive halos in the $N(V_{\rm circ})\Delta V_{\rm circ}$ histograms. (1) The results are sensitive to the choice of R used to compute the circular velocities—this is obvious since the circular velocity profiles are not flat for the massive halos. (2) We have shown that higher resolution DENMAX grids reveal more substructure in some of the massive halos found in the higher force resolution simulations. However, from the images it appears that no obvious substructure is present in many of the massive halos. (3) Lower resolution DENMAX grids include more peripheral particles in the halos than higher resolution DENMAX grids. This arbitrary choice of DENMAX grid does not affect most computations of circular velocities. It does, however, affect the computations of total bound masses; this explains why the CMF is more sensitive to the limitations of the current version of DENMAX than is the case for the circular velocities. (4) FOF($l = 0.2$) occasionally links together visually distinct halos. FOF($l = 0.1$) and FOF($l = 0.2$) produce similar results for many of the massive halos but they often fail to match up with DENMAX results which, visually, appear to do a good job in many cases. (5) The P^{3}M simulations produce halos that are more compact than the PM simulations. However, if a larger value of R is chosen for the PM simulations, then the PM circular velocities agree with the P^{3}M circular velocities in most cases.

4.4. *Massive Halos: Simulations versus Observations*

The distribution of simulated halos with circular velocities in the range 150 km s^{-1} $\lesssim V_{\rm circ} \lesssim$ 350 km s^{-1} is in reasonable agreement with observations (Fig. 15). However, there are too many halos with circular velocities exceeding 350 km s^{-1}. A simulation with increased force resolution can reveal more substructure in massive halos and a continuum-limit DENMAX algorithm would be helpful for analyzing such simulations. We take the approach, in this paper, that these massive dark matter halos represent single, large galaxies. The possibility that they may represent clusters is studied in detail in Paper II.

We use fairly complete catalogs of observed bright ellipticals to estimate their number density. It is not accurate enough to estimate the brightest, relatively few elliptical galaxies simply from a Schechter luminosity function and a Faber-Jackson relationship. The problem is exacerbated by the large amount of scatter relating σ_1 to $V_{\rm circ}$ for the simulated massive halos. In this subsection we instead use σ_r to characterize the simulated massive halos, and we compare them with the number of observed ellipticals using complete elliptical surveys. We use these comparisons to constrain the normalization of the $\Omega = 1$ CDM power spectrum using the fact that as the simulations evolve, merging creates more massive halos.

We begin by noting that there are observed galaxy halos that have large measured circular velocities beyond $\sim$100 kpc. The giant elliptical galaxy M87 has been studied by many workers using the X-ray–emitting gas to trace the gravitational potential well (e.g., Fabricant & Gorenstein 1983; White & Sarazin 1988; Tsai 1994). Tsai (1994) modeled the X-ray emission from M87 using a multiphase gas assumed to be in hydrostatic equilibrium. Tsai found the best-fit gas temperature and mass density profile consistent with both X-ray continuum and line emission data. His results are consistent with the velocity dispersions of Sargent et al. (1978) and Mould et al. (1990) on small scales. (Note that the mean, radial velocity dispersion, σ_r, of stars in M87 from 1 kpc to 4.5 kpc is roughly constant at only 278 $\pm$ 11 km s^{-1}, yet can be as high as 350 km s^{-1} well within 1 kpc—cf. Sargent et al.) The inferred mass within 300 kpc assuming a Hubble constant of 50 km s^{-1} Mpc^{-1} is approximately 2.5 $\times$ 10^{13} $M_\odot$ with a corresponding circular velocity of 592 km s^{-1}. Curiously, 1.1 $\times$ 592 km s^{-1}/ $3^{1/2}$ = 376 km s^{-1} (see eq. [3.8]) which is close to the 350 km s^{-1} measurement (within 1 kpc) from Sargent et al. (1978). However, since it is not clear which small-scale star measurements should be related to large-scale dark matter measurements, we adopt an empirical scaling law which relates Faber et al. (1989) central velocity measurements (used as a complete catalog of nearby ellipticals) to Tsai (1994) circular velocity measurements on large scales.

In Figure 19 we show circular velocity profiles for halos B and C (see Tables 2 and 3) from the simulations at $\sigma_8 = 0.5$ and for M87 (Tsai 1994). We choose halo C because it has a circular velocity comparable to M87 at large radii. (Halo B has a higher circular velocity than M87.) The profiles from PM CDM 1 rise slowly which is expected since the force softening is 280 kpc comoving. The profiles from P^{3}M CDM 12 rise more quickly than PM CDM 1 because of higher force resolution. Ignoring the fact that many of the simulated halos are still rising beyond 150 kpc comoving, the conjecture that at least some of the very massive simulated halos are similar to objects like M87 is seen to be plausible.

We offer a possible explanation why the simulated rotation curves are still rising beyond the softening scale for P^{3}M CDM 12 while M87 has a very flat rotation curve. During the dissi-

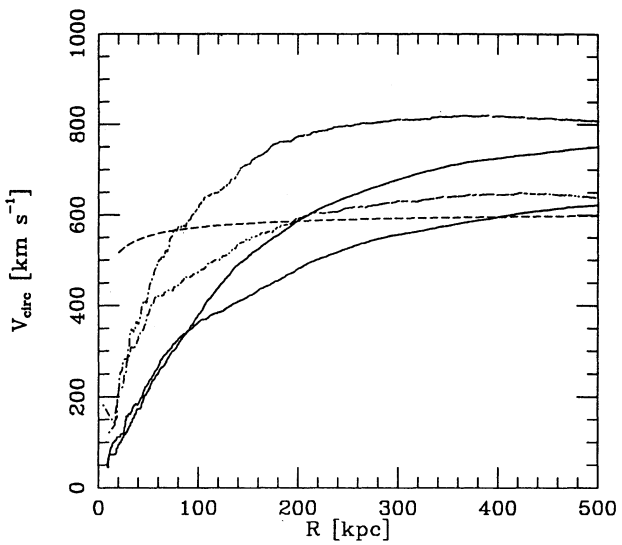

FIG. 19.—The circular velocity profiles at $\sigma_8 = 0.5$ for halos B and C (halo B has a larger $V_{\rm circ}$ than halo C) from CDM 1 (*solid curves*: 128^3, 51.2, 280; see Table 3) and from CDM 12 (*dotted curves*: 64^3, 51.2, 52; see Table 2). We show the profile for M87 as computed by Tsai (1994) based on analysis of X-ray emission (*short-dashed curve*).

pational formation of M87, dark matter can be pulled into the central region by baryonic infall (e.g., Blumenthal et al. 1986). If we examine $V_{circ}(r)$ in Figure 3 from Blumenthal et al. (though from a system with maximum circular velocity ~ 200 km s^{-1}), we estimate that the ratio of the distances where V_{circ} turns over is ~ 80 kpc/10 kpc = 8. For the P^{3}M CDM 12 halo C profile shown in Figure 19, this effect could possibly "pull" the turnover in the dark matter rotation curve from ~ 200 kpc to ~ 25 kpc, consistent with the turnover in the M87 profile shown in Figure 19.

We examine the largest halos found in the simulations and we compare them to one of the most massive and luminous galaxies known—the central cD galaxy in the cluster A2029 (Dressler 1979; Uson, Boughn, & Kuhn 1991). The mass profile of this galaxy has been estimated with a three-component model by Dressler (1979): (1) a "normal" elliptical galaxy; (2) an extended halo of luminous material out to 100 kpc; and (3) a dark cluster-filling component. Dressler estimated the mass within 100 kpc (for $H_0 = 50$ km s^{-1} Mpc^{-1}) to be $\sim 3.9 \times 10^{13}\ M_\odot$ and with 1 Mpc to be $\sim 8.3 \times 10^{15}\ M_\odot$. The evidence that the material within 100 kpc is part of the central cD galaxy is strong, but there is some controversy about the mass out to 1 Mpc. Uson et al. have argued that the material out to 1 Mpc and beyond is indeed part of the central cD galaxy. They measure diffuse light out to several Mpc. They found that it has an elliptical profile with the same axis ratio and orientation as the central cD galaxy, and that this is different from the distribution of the cluster galaxies as a whole.

To compare with the above measurements, we compute the mass within 100 kpc comoving and 1 Mpc comoving from the simulated halos. Using CDM 12(64^3, 51.2, 52) we find the halo with the largest mass within 100 kpc comoving and the halo with the largest mass within 1 Mpc comoving. The results within 100 kpc comoving (more than twice the Plummer softening) are $9.0 \times 10^{12}\ M_\odot$ at $\sigma_8 = 0.5$, $1.7 \times 10^{13}\ M_\odot$ at $\sigma_8 = 0.7$, and $2.9 \times 10^{13}\ M_\odot$ at $\sigma_8 = 1.0$. None of these is greater than Dressler's estimate for the central cD galaxy in A2029, $3.9 \times 10^{13}\ M_\odot$. Within 1 Mpc comoving we find $1.3 \times 10^{14}\ M_\odot$ at $\sigma_8 = 0.5$, $1.9 \times 10^{14}\ M_\odot$ at $\sigma_8 = 0.7$, and $1.9 \times 10^{14}\ M_\odot$ at $\sigma_8 = 1.0$. Again, these are all smaller than Dressler's estimate, $8.3 \times 10^{15}\ M_\odot$. Thus we cannot rule out CDM by arguing that it produces halos with absolutely too much mass. We also cannot rule out CDM merely by the fact that our simulation fails to make at least one halo as massive as the central cD galaxy in A2029—we sample only a 51.2 Mpc box while A2029 is at a distance of 470 Mpc.

We examine other simulations in an attempt to find halos as massive as the central CD galaxy in A2029. We examine CDM 6(256^3, 51.2, 190) at $R = 1$ Mpc comoving at $\sigma_8 = 1.0$. The most massive halo at this radius has a mass of $3.7 \times 10^{14}\ M_\odot$. Also, we examine CDM 16(144^3, 100, 85) at $\sigma_8 = 1.0$ with no cut in radius, and the most massive halo has a mass of 8.9×10^{14}. This is a larger box with larger waves in the initial conditions and a different set of initial random numbers. The model still fails to produce a halo as massive as $\sim 8.3 \times 10^{15}\ M_\odot$. Thus far the $\Omega = 1$ CDM model may be safe.

Although we cannot reject CDM based on the most massive halo in the simulations, may be we can reject it based on the large number of slightly less massive halos that are formed. Because the most massive galaxies are ellipticals, we compare the number of simulated halos with large radial velocity dispersion σ_r (second of eqs. [3.1]) with the number of ellipticals having large line-of-sight central velocity dispersion. For the observations we use the samples of nearby bright elliptical galaxies from Faber et al. (1989) and from the Dressler (1991) supergalactic plane redshift survey. We count the number of ellipticals in these samples with $\log_{10} \sigma_r \geq 2.5$ (20 ellipticals). We then impose a distance cut of 6000 km s^{-1} (based on corrected distances from col. [12] of Table 3 from Faber et al. 1989). This leaves 14 ellipticals. The samples are fairly complete. For the range in apparent magnitudes of our list of ellipticals, the completeness fraction ranges from 100% for $B_T \lesssim 11.6$ down to 20% for ellipticals in the southern sample with $B_T \sim 13$. If we fold in the completeness fractions (Fig. 2 for Faber et al. 1989) the number of 14 ellipticals with $\log_{10} \sigma_r \geq 2.5$ within a distance of 6000 km s^{-1} might be as high as ~ 23.

We also estimate the number of observed ellipticals from the above samples with $\sigma_r \geq 350$ km s^{-1}. This allows us to study very high values of σ_r, for which the completeness fractions are much higher. Within 6000 km s^{-1} there are only three known galaxies with $\sigma_r \geq 350$ km s^{-1}: SPS 1120 ($\sigma_r = 382$ km s^{-1}; $B_T = 12.68$), NGC 507 ($\sigma_r = 366$ km s^{-1}; $B_T = 11.63$), and NGC 4486 (M87; $\sigma_r = 361$ km s^{-1}; $B_T = 9.52$). The completeness fraction (based on B_T) for SPS 1120 is $\sim 30\%$ and the completeness fraction for the other two objects is 100%. This tightly constrains the number of observed ellipticals with $\sigma_r \geq 350$ km s^{-1} within 6000 km s^{-1} to 5.

To demonstrate the inaccuracies at the high-mass end associated with methods presented in § 3, we compare the above complete estimates with the use of the Faber-Jackson relationship (eq. [3.7]) using σ_1 (first of eqs. [3.1]) and the Schechter function described in § 3. Again, we weight the Schechter function by 30%; i.e., we only estimate the elliptical contributions. We find in a spherical volume of radius 120 Mpc comoving: 39 objects with $\sigma_1 \geq 316$ km s^{-1} and 11 objects with $\sigma_1 \geq 350$ km s^{-1}. These numbers are about a factor of 2 larger than the estimates given above, suggesting that our assmed Faber-Jackson relation underestimates the luminosity and/or that ellipticals make up less than 30% of bright galaxies. (We combine ellipticals and lenticulars in getting the population fraction of 30%, but lenticulars are underrepresented among the most massive galaxies.) In any case, these results suggests that we have overestimated the observed $N(V_{circ})$ in Figures 13 through 16 for $V_{circ} \gtrsim 500$ km s^{-1}, making the disagreement with the simulations even worse.

To make a better comparison of the simulations with observations, we estimate the number of simulated halos from four simulations with $\sigma_r \geq 316$ km s^{-1} and $\sigma_r \geq 350$ km s^{-1}. The results are shown in Table 4 for simulations with a variety of force resolution and mass resolution. All numbers are scaled to a (51.2 Mpc)^3 comoving volume. The observations are shown as OBS I (without completeness fractions folded in) and as OBS II (with completeness fractions folded in). All simulations use a 51.2 Mpc box except for CDM 16 which uses a 100 Mpc box. The initial conditions for CDM 6, CDM 1, and CDM 12 are all generated from the same set of 256^3 random numbers. The initial conditions for CDM 2–5 and CDM 16 are all generated from different sets of random numbers. We also show averages, with 1 σ fluctuations, computed from CDM 1–5.

We estimate the velocity dispersions from the simulated halos in two ways: σ_r and $\tilde{\sigma}$ which we describe below. We compute the radial velocity dispersion, second of equations (3.1), within a radius listed in the footnotes of Table 4. We count the number of halos with σ_r exceeding 316 km s^{-1} and 350 km s^{-1}. We also try using σ_1 (not shown), first of equations (3.1), and the results are similar to the results using σ_r (the

TABLE 4

NUMBER OF MASSIVE HALOS SCALED TO 51.2 MPC BOX

SAMPLE[a]	σ_8	σ_r[b] ≥ 316 km s^{-1}	$\tilde{\sigma}$[c] ≥ 316 km s^{-1}	$\sigma_r \geq 350$ km s^{-1}	$\tilde{\sigma} \geq 350$ km s^{-1}
OBS I[d]	...	0.26 (14)	...	0.056 (3)	...
OBS II[e]	...	0.43 (23)	...	0.093 (5)	...
CDM 12	0.3	1	0	1	0
CDM 12	0.4	6	1	4	1
CDM 6	0.5	12	5	9	3
CDM 12	0.5	12	2	7	2
CDM 1	0.5	5	4	4	2
⟨CDM 1–5⟩[f]	0.5	5.8 ± 1.5	4.0 ± 1.2	3.4 ± 0.9	1.8 ± 0.8
CDM 16	0.5	11.0	3.0	6.7	1.7
CDM 6	0.7	20	11	13	6
CDM 12	0.7	20	7	13	3
CDM 1	0.7	7	6	4	5
⟨CDM 1–5⟩	0.7	10.4 ± 3.4	8.0 ± 2.0	6.4 ± 1.8	4.8 ± 1.1
CDM 16	0.7	16.6	10.5	12.0	5.9
CDM 6	1.0	39	26	33	19
CDM 12	1.0	28	19	23	15
CDM 1	1.0	16	15	11	11
⟨CDM 1–5⟩	1.0	13.6 ± 2.3	15.0 ± 2.1	11.2 ± 2.2	11.2 ± 0.8
CDM 16	1.0	20.7	17.7	16.0	13.2

[a] Comoving radial cutoff, R, used to compute dispersions: 300 kpc for CDM 6, 100 kpc for CDM 12, 300 kpc for CDM 1–5, and 150 kpc for CDM 16.

[b] Radial one-dimensional velocity dispersion, σ_r, second of eqs. (3.1).

[c] Estimate of σ_r from $V_{\rm circ}$: $\tilde{\sigma} \equiv 361$ km s^{-1} $\times$ $V_{\rm circ}(R)/600$ km s^{-1}.

[d] Observational estimates *without* completeness fractions. Numbers in parentheses are for 6000 km s^{-1} sphere.

[e] Observational estimate *with* completeness fractions. Numbers in parentheses are for 6000 km s^{-1} sphere.

[f] Average from five simulations with 1 σ errors.

differences arise from the fact that σ_1 is typically $\sim 20\%$ lower than σ_r as mentioned earlier).

The high velocity dispersions of the dark matter may not correspond to the velocity dispersions of the optical galaxies expected to be embedded well within the cutoff radii used here. As a crude estimate of the central velocity dispersion of a galaxy expected to be embedded in the simulated halo, we use the following: $\tilde{\sigma} \equiv 361$ km s^{-1} $\times$ $V_{\rm circ}(R)/600$ km s^{-1}. We choose this because the central velocity dispersion of M87 is 361 km s^{-1} from Faber et al. (1989) and the estimated circular velocity profile for M87 (from Tsai 1994; see Fig. 19) is about 600 km s^{-1} for $R \gtrsim 100$ kpc. Admittedly this is a crude estimate, but it is a simple attempt to use a single, well-measured object to scale the simulated data, and it serves as a conservative check for our comparisons with observations. (Note, in this case eq. [3.8] works fairly well for $F = 1.1$. However, it may not work well for all objects.)

In Table 4 we compare the results from the simulations with the observations. The most important conclusion is that all cases for $\sigma_8 \gtrsim 0.4$ yield far more halos than the observed numbers. The epoch $\sigma_8 = 0.3$ is not ruled out since it is difficult to make conclusions based on zero or one halo. The results at $\sigma_8 = 0.4$ indicate that there are too many halos with $\sigma_r \geq 316$ km s^{-1}. The problem is less severe (yet not an order of magnitude different from σ_r) using $\tilde{\sigma}$, but the observations tell us that even a single halo with $\sigma_r \geq 350$ km s^{-1} in a 51.2 Mpc box is too high by at least a factor of 10.

White et al. (1987), at $\sigma_8 = 0.4$ using the same normalization of the CDM power spectrum as we do, found a single halo with a circular velocity exceeding 800 km s^{-1} in a 50 Mpc box from three simulations, corresponding to 0.36 halos for a single 51.2 Mpc simulation. Our CDM 12 simulation has nearly identical force and mass resolution. Our largest halo in CDM 12 at $\sigma_8 = 0.4$ has a circular velocity of 567 km s^{-1} defined at 100 kpc comoving. We cannot safely rule out $\sigma_8 = 0.4$ particularly since results using $\tilde{\sigma}$ only reveal one very massive halo. The problem becomes rapidly worse for larger σ_8; $\sigma_8 \gtrsim 0.7$ predicts more than 20 times too many galaxies with $\sigma_r \geq 350$ km s^{-1}. This is a severe problem for $\Omega = 1$ CDM since estimates of σ_8 based on clustering typically require $\sigma_8 \gtrsim 0.4$ (Davis et al. 1985; Park 1990; Couchman & Carlberg 1992).

We now compare the different simulations with each other. We see the general trend, in Table 4, that both an increase in mass resolution and an increase in force resolution increase the production of massive halos. For the simulations using equivalent initial conditions (CDM 6, CDM 12, and CDM 1) we examine corresponding massive halos. The higher force resolution simulations produce more compact halos than the lower force resolution simulations; the cutoff radius is chosen to compensate for this fact for reasons discussed earlier. In some cases, however, the cutoff radius does not compensate for the compactness of the high force resolution halos. We also find that the high force resolution halos have higher central velocity dispersions.

An increase in mass resolution also increases the production of massive halos. The effect is strongest at $\sigma_8 = 1.0$, where the numbers from the 256^3 particle simulation are far higher than the other simulations compared with earlier epochs. We observe that the results from the 100 Mpc box simulation CDM 16 with good mass and force resolution are in reasonable agreement with the other simulations except at $\sigma_8 = 1$. We also observe that the 128^3 particle, $R_{1/2} = 280$ kpc com-

oving PM simulations produce the smallest number of massive halos—these simulations rank low in the combination of force and mass resolution and $R = 300$ kpc comoving is too close to $R_{1/2} = 280$ kpc comoving.

We conclude that the $\Omega = 1$ CDM model is in serious trouble. The simulations produce far too many massive halos and an increase in force and mass resolution only make matters worse. We are able to rule out all normalizations of the primeval density fluctuations with $\sigma_8 \gtrsim 0.5$. Using complete catalogs of nearby bright ellipticals, we have constrained the CDM model more convincingly than by using the luminosity function at the bright end (cf. Fig. 15 and Frenk et al. 1988). The case against $\sigma_8 = 0.4$ is not as strong as the case against $\sigma_8 \gtrsim 0.5$. We found, at the very least, a single halo with an estimated central velocity dispersion exceeding 350 km s^{-1} in a single 51.2 Mpc box simulation. The observations predict that we should only find one such object in no fewer than 11 simulations.

We know that the simulations suffer from the overmerging of massive halos. Gas dynamical dissipation could reduce the merging of galaxies. The result might be to prevent the formation of excessively massive galaxies, although we consider this unlikely because dissipation should only increase the central concentration of mass in the most massive halos, thereby increasing further the central velocity dispersions. Also, if the most massive halos actually should represent clusters of galaxies, then these clusters must still have the correct multiplicity function (distribution of richness). Bahcall & Cen (1992) concluded that the CDM model with $\sigma_8 = 1.05$ produces an order of magnitude too many rich clusters. In Paper II we investigate the cluster multiplicity function in detail using our own high-resolution N-body simulations.

4.5. *Low-Mass Halos*

We now examine the low-mass halos. We found earlier that the P^{3}M simulations produce too many halos with $V_{\rm circ} \lesssim 150$ km s^{-1} (see Fig. 15). Frenk et al. (1988) argue that the number of halos is in reasonable agreement with the observations down to about 60 km s^{-1} using 32,000 particle P^{3}M simulations in 14 Mpc boxes. However, they warned the reader that simulations in larger volumes predict too many halos (White et al. 1987). The particle mass in the Frenk et al. simulations is $5.8 \times 10^9\ M_\odot$ and the force resolution is $\epsilon = 14$ kpc. We have two P^{3}M simulations with lower mass and force resolution that are computed in a 51.2 Mpc box and a 100 Mpc box giving us better statistics: CDM 12(64^3, 51.2, 52; $m_{\rm part} = 3.5 \times 10^{10}\ M_\odot$; $\epsilon = 40$ kpc comoving) and CDM 16(144^3, 100, 85; $m_{\rm part} = 2.3 \times 10^{10}\ M_\odot$; $\epsilon = 65$ kpc comoving). Using these simulations, we explore the effects of resolution and we reexamine the observational data at the low-mass end in order to explore the apparent excess number of low-mass halos compared with the observations.

The smallest galaxies for which there are reliable mass estimates have $V_{\rm circ}$ down to about 50 km s^{-1} (see Kormendy 1990, and references therein). Halos from the 40 kpc comoving Plummer simulation CDM 12 with a cutoff radius of 100 kpc comoving (roughly twice the Plummer softening) and five particles have a circular velocity of 87 km s^{-1}. Halos from the 65 kpc comoving Plummer simulation CDM 16 with a cutoff radius of 150 kpc comoving and five particles have a circular velocity of 70 km s^{-1}. Therefore, we can study only halos down to 70 km s^{-1} using the P^{3}M simulations.

Halos from the PM simulation CDM 1(128^3, 51.2, 280) with five particles and a cutoff radius of 300 kpc comoving have a circular velocity of 18 km s^{-1}, and halos from the PM simulation CDM 6(256^3, 51.2, 190) with 25 particles and a cutoff radius of 300 kpc comoving have a circular velocity of 14 km s^{-1}. However, these PM simulations have poor force resolution. We show that higher force resolution increases the number of low-mass halos. Therefore it is misleading to compare the number of low-mass halos with the observations using the PM simulations.

Another problem stems from the fact that we need to use large cutoff radii to characterize the circular velocities in PM simulations. In order for a galaxy to undergo "complete collapse" in a spherical, $\Omega = 1$ model, it has to have an overdensity exceeding $\delta_g = \delta\rho/\rho \sim 170$ (Gunn & Gott 1972; BBKS). A similar calculation shows that this places a lower limit on the circular velocity for a given cutoff radius R. The circular velocity within R for a density ρ is simply

$$V_{\rm circ}(R) = \left[\frac{G(4/3)\pi R^3 \rho}{R}\right]^{1/2} . \tag{4.1}$$

If we demand that the overdensity exceed $\delta_g = \rho/\rho_{\rm crit} - 1$, where $\rho_{\rm crit}$ is the density for an $\Omega = 1$ universe given by $3H_0^2/(8\pi G)$, we get the minimum allowed circular velocity:

$$V_{\rm circ}(R) = \left(\frac{\delta_g + 1}{2}\right)^{1/2} H_0 R . \tag{4.2}$$

For $\delta_g = 200$ (close to the critical value, chosen to yield a simple formula), $H_0 = 50$ km s^{-1} Mpc^{-1}, and a comoving cutoff radius R measured in kpc, we arrive at the simple formula for the minimum allowed circular velocity in km s^{-1}:

$$V_{\rm circ}(R) \approx \frac{1}{2}\left(\frac{R}{\rm kpc}\right) \text{km s}^{-1} . \tag{4.3}$$

Equation (4.3) puts a severe limit, $V_{\rm circ} \gtrsim 150$ km s^{-1}, on the PM simulations that require $R = 300$ kpc comoving. For the P^{3}M simulations that require $R = 100$ kpc comoving and 150 kpc comoving, the restrictions are 50 km s^{-1} and 75 km s^{-1}, respectively.

Before exploring the simulations, we need to examine the observational parameters used for the Tully-Fisher relationship and the Schechter luminosity function (see § 3) for faint galaxies. Since we have already shown that the simulations appear to produce too many halos at the low-mass end, we conservatively choose parameters that produce the largest number of low-mass halos allowed within the uncertainties of the observations. (We find that there are still too many halos predicted by the CDM model so we are not forcing the observations to agree with the model—we are simply estimating how significant is the discrepancy.) In the following discussion we rescale all relevant numbers to a Hubble constant $H_0 = 50$ km s^{-1} Mpc^{-1}.

First we consider the Tully-Fisher relationship in equation (3.6). Pierce & Tully (1988) reported that the scatter in this relationship is ± 0.25 mag. In their fits (Fig. 9 from their paper), they found that the faintest galaxy studied, $M_{B_T} \approx -16 + 5 \log_{10}(50/85) \approx -17.2$, is slightly brighter than predicted by their best fit. Alternatively, if one measures the circular velocity of this faint galaxy, the Pierce & Tully relationship would predict that the galaxy is fainter than it actually is. Since the

luminosity function is an increasing function of decreasing luminosity, one would overestimate the number of faint galaxies. We take an extreme point of view. We will use equation (3.6) as is with an added value of 0.5 mag—this is twice the reported scatter quoted by Pierce & Tully and it results in an increase in the estimate for the number of observed halos as a function of $V_{\rm circ}$.

Next, we consider the luminosity function. The estimates of Efstathiou (1988a) for the parameters of the luminosity function are estimated to hold down to about $M_{B_T} \approx -16 + 5 \log_{10}(50/100) \approx -17.5$. The luminosity function has been studied by previous workers down to comparably faint magnitudes (see Felten 1977 for a review). This faint limit is comparable to the faint limit of the Tully-Fisher relationship. Therefore, we use the parameters of the Schechter luminosity function given in § 3 but we use the reported errors to yield the maximum number of faint galaxies. We assume that 100% of the faint galaxies are spirals. We use $\Phi^* = (1.56 + 0.34) \times 10^{-2} h^3$ Mpc^{-3} and $M^*_{B_T} + (-19.68 - 0.10) - 2.5 \log_{10} h^{-2}$ with $h = \frac{1}{2}$ and we use $\alpha = -1.07 - 0.05$.

These changes in the Tully-Fisher relationship and the Schechter luminosity function increase the estimated number of faint halos with 50 km s^{-1} $\leq V_{\rm circ} <$ 75 km s^{-1} from 373 to 582 galaxies in a (51.2 Mpc)^3 comoving volume. When we show the number of observed low-mass halos, we use both the parameters given in § 3 and the extremely stretched parameters given in this section.

In Figures 20 and 21 we show the low-mass end, 50 km s^{-1} $\leq V_{\rm circ} <$ 200 km s^{-1}, from the simulations. We still use 25 km s^{-1} wide bins but we rebin the data from 50 km s^{-1} to 75 km s^{-1}, 75 km s^{-1} to 100 km s^{-1}, etc. The observations using the parameters described in § 3 with $F = 1$ are shown as solid squares. The "maximum" number of faint halos allowed by the observations minus the default values is used for the $\pm$ error bars (the asymmetry is because we use logarithms on the vertical axes; note these are not 1 σ error bars).

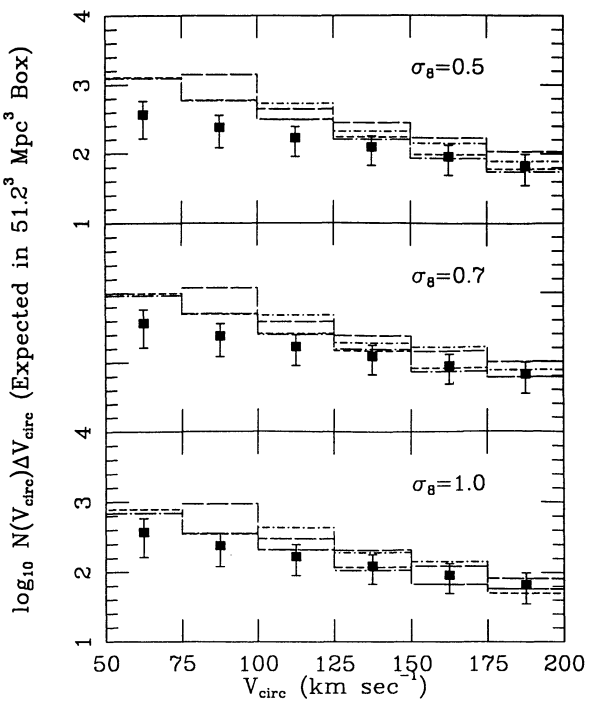

FIG. 20.—Distributions of simulated low-mass halos from four simulations with various comoving cuts R: CDM 1(128^3, 51.2, 280, R = 300 kpc; *dot-long-dashed histograms*), CDM 6(256^3, 51.2, 190, R = 300 kpc; *short-dashed histograms*), CDM 16(144^3, 100, 85, R = 150 kpc; *long-dashed histograms*), and CDM 12(64^3, 51.2, 52, R = 100 kpc; *dot-short-dashed histograms*). We estimate the observed numbers using parameters presented in § 3 (*solid squares*) with plus/minus error bars (these are "extreme" systematic errors, not 1 σ error bars).

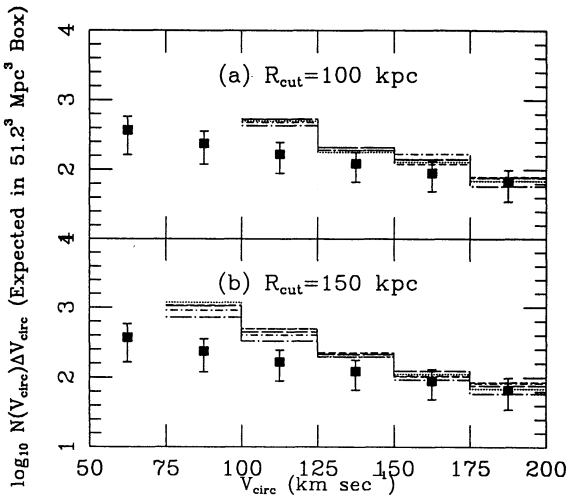

FIG. 21.—Distributions of simulated low-mass halos from CDM 12(64^3, 51.2, 52). (The observed numbers are solid squares with error bars, see Fig. 20.) The results are shown for (*a*) R = 100 kpc comoving and (*b*) R = 150 kpc comoving. The results are shown at $\sigma_8 = 0.3$ (*dotted histograms*), 0.4 (*short-dashed histograms*), 0.5 (*long-dashed histograms*), 0.7 (*dot-short-dashed histograms*), and 1.0 (*dot-long-dashed histograms*).

The figures list the various simulation parameters and the choices of R. The simulations are shown down to circular velocities such that the bins are complete given the mass resolution limit. These restrictions exceed the restrictions based on the overdensity argument, equation (4.3), for the P^{3}M simulations. The PM simulations are restricted by the overdensity argument to $V_{\rm circ} \gtrsim 150$ km s^{-1}. The PM simulations produce fewer low-mass halos than the P^{3}M simulations. This must not be taken to mean better agreement; instead it is an example of how poor force resolution can give misleading results.

The results for the $\epsilon = 40$ kpc comoving Plummer simulation, CDM 12, and the $\epsilon = 65$ kpc comoving Plummer simulation, CDM 16, are in reasonable agreement with each other above 100 km s^{-1}. CDM 16 has slightly more power on small scales, $\lambda_{\rm Nyquist} = 2\pi/k_{\rm Nyquist} = 2 \times$ (100 Mpc/144), than does CDM 12, $\lambda_{\rm Nyquist} = 2 \times$ (51.2 Mpc/64). We learned from the CMF studies (§ 2.3) that small-scale waves affect the low-mass end.

In Figure 21 we show results from CDM 12 for R = 100 kpc comoving and 150 kpc comoving at σ_8 = 0.3, 0.4, 0.5, 0.7, and 1.0. We see that the results are not very sensitive to R. In all cases, there are still too many halos particularly below 125 km s^{-1} and definitely below 100 km s^{-1}. We see that the number of low-mass halos, unlike the high-mass halos, decreases with increasing expansion factor (both effects are due to merging).

We now compare a few numbers at $\sigma_8 = 0.4$ and $\sigma_8 = 1.0$ from CDM 12 (with R = 150 kpc comoving) for the ranges 75 km s^{-1} $\leq V_{\rm circ} <$ 100 km s^{-1} and 100 km s^{-1} $\leq V_{\rm circ} <$ 125 km s^{-1}. The numbers in these bins from the simulation are

1087 and 495, respectively, for $\sigma_8 = 0.4$ and 724 and 333, respectively, for $\sigma_8 = 1.0$. Using the observational parameters from § 3 we find 240 and 168, respectively. Using the extreme observational parameters discussed in this section boosts the numbers to 360 and 247, respectively. Therefore, the excess number of halos below $V_{circ} \sim 125$ km s^{-1} is significant. The simulations produce factors $\sim$2–3 too many faint halos. As a final check, we use the parameters described in this section but we try $\alpha = -1.25$ which boosts the number for 75 km s$^{-1} \leq V_{circ} < 100$ km s^{-1} to 553—still short of the 724–1087 found in the simulation.

We conclude that the $\Omega = 1$ CDM model produces too many low-mass halos compared with the observations for $V_{circ} \lesssim 125$ km s^{-1}. We have compared the numbers from a 40 kpc comoving Plummer simulation with the largest estimates allowed by the observations and the discrepancy is still large (about a factor of 2). Increased force resolution and increased small-scale power in the initial conditions make the disagreement worse. Although these disparities are large, Dekel & Silk (1986) argued that supernovae in dwarf galaxies can cause significant gas loss, and therefore dim the galaxies with small V_{circ}. Perhaps the Tully-Fisher relation breaks down at such small V_{circ} (though there is little indication of this in the data of Pierce & Tully 1988). For these reasons, though, we consider the excessive number of low-mass halos in the CDM model to be less serious than the excessive number of high-mass halos.

5. CONCLUSIONS

A promising result for the CDM model is that the distribution of halos as a function of circular velocity agrees rather well with the observations for circular velocities in the range 150 km s^{-1} to 350 km s^{-1}. The agreement is better over this range for the P^{3}M simulations versus the lower force resolution PM simulations and the agreement is not very sensitive to a Plummer softening of 40 kpc comoving versus 65 kpc comoving over this range. However, we found serious problems outside of this range and the problems are made worse by increasing the force resolution and the mass resolution. Although CDM 16 is not the highest resolution simulation, it is computed in a 100 Mpc box; we will discover in Paper II that 51.2 Mpc boxes are too small to accurately study clustering. On the other hand, the properties of individual halos are not very sensitive to the differences between a 51.2 Mpc box and a 100 Mpc box—this fortunate fact allowed us to use many of the 51.2 Mpc box simulations to explore effects arising from varying mass and force resolution and from different methods for identifying halos.

We now summarize the chief conclusions found in the preceding sections.

1. We studied the cumulative mass fraction CMF(M), the fraction of all the mass in halos more massive than M. We found the following: (*a*) we need to compare the CMF from simulations analyzed with the same effective DENMAX resolution—lower resolution grids include more peripheral particles, increasing the total masses of the halos; (*b*) the simulation-to-simulation scatter is small except for the most massive halos; (*c*) higher mass resolution and higher force resolution each increase the CMF independently. The effect of increased mass resolution on the CMF is reduced if we impose a distance cut from the density peaks of the halos, and comparisons of simulations with 64^3, 128^3, and 256^3 particles indicate that the convergence of the CMF with such a cut is plausible; (*d*) small-scale waves in the initial conditions have a very small effect on the CMF except for the smallest halos; (*e*) long waves (with wavelength exceeding 51.2 Mpc comoving) in the initial conditions do not affect the CMF for amplitude $\sigma_8 \leq 0.5$; and (*f*) the Press-Schechter theory with $\delta_c = 1.68$ predicts too many massive halos and a more rapid growth of the CMF than found in the simulations. Substructure within halos is apparently not erased as rapidly as implied in the Press-Schechter theory.

2. Simulated halos generally have mass distributions characterized by flat rotation curves extending from about two softening radii to 500 kpc comoving or more. The most massive halos have shallower density profiles, resulting in rising rotation curves. The independence of circular velocity with radius for most halos allows us to compare simulated halos at radii of 150–200 kpc comoving (in the P^{3}M simulations) with real spirals at 10 kpc comoving or less.

3. The distribution of circular velocities of simulated halos was compared with observations. We noted above the good agreement for 150 km s$^{-1} \lesssim V_{circ} \lesssim 350$ km s^{-1} for any of the three normalizations $\sigma_8 = 0.5$, 0.7, and 1.0. In the analysis, *for this range in circular velocities*, we found the following: (*a*) The agreement with the observations is best for the P^{3}M simulations and is not very sensitive to simulations with a Plummer softening of 40 kpc comoving versus 65 kpc comoving. (*b*) The results from DENMAX agree better with FOF($l = 0.2$) than with FOF($l = 0.1$). (*c*) The distribution of circular velocities, unlike the CMF, is not very sensitive to the DENMAX grid, but higher resolution grids are required to pick out substructure in the P^{3}M simulations. (*d*) The number of halos characterized by their circular velocities (using a fixed, physical radius) indicates, if $\sigma_8 = 1$ is the present epoch, that the galaxy mass function takes on its present shape by $z \sim 3.7$. Between this epoch and $z = 0$, merging reduces the number of halos by about a factor of 3.7. Merging is predicted to continue into the future.

4. We conclude from the studies of massive halos that the $\Omega = 1$ CDM model is in trouble if these systems represent individual galaxy halos. We are able to rule out normalizations of the primeval density fluctuations with $\sigma_8 \gtrsim 0.4$ based on the number of massive halos if the halos represent individual galaxies, although the lower limit for σ_8 is uncertain. We compared the simulations not only with the observed luminosity function, but also with complete samples of bright nearby ellipticals. These observations constrain the model to $\sigma_8 \lesssim 0.5$. We cannot rule out CDM based on the most massive halo—we do not find any halos at any epochs with masses exceeding the inferred mass of the central cD galaxy in A2029. If the massive halos represent unresolved clusters, with the central galaxy having a smaller central velocity dispersion than the surrounding halo, we may relax these constraints. We consider this possibility further in Paper II.

5. We conclude from the low-mass studies that the $\Omega = 1$ CDM model produces too many low-mass halos (by factors $\sim$2–3) compared with the observations for $V_{circ} \lesssim 125$ km s^{-1}. The number of faint halos decreases with increasing σ_8 because of merging. Nevertheless, the excess is significant even at $\sigma_8 = 1$ using extreme assumptions about the observational uncertainties. We do not find reasonable agreement down to $\sim$60 km s^{-1} as reported by Frenk et al. (1988). Gas loss in dwarf galaxies (Dekel & Silk 1986), however, might dim a significant number of dwarf galaxies, making this problem less critical for CDM than the high mass problem.

This research was conducted using the Cornell National Supercomputer Facility, a resource of the Center for Theory and Simulation in Science and Engineering at Cornell University, which receives major funding from the National Science Foundation and IBM Corporation, with additional support from New York State and members of its Corporate Research Institute. We appreciate the IBM 3090 programming assistance of CNSF consultant Paul Schwarz. We thank John Tsai for providing his estimated mass profile for M87 in advance of publication. We thank Paul Schechter for useful suggestions. This work was supported by NSF grant AST 90-01762 and in part by the DOE and NASA at Fermilab through grant NAGW-2381.

REFERENCES

Adams, F. C., Bond, J. R., Freese, K., Frieman, J. A., & Olinto, A. V. 1993, Phys. Rev. D, 47, 426
Bahcall, N., & Cen, R. 1992, ApJ, 398, L81
Bardeen, J. M., Bond, J. R., Kaiser, N., & Szalay, A. S. 1986, ApJ, 300, 15 (BBKS)
Bertschinger, E. 1991, in After the First Three Minutes, ed. S. Holt, V. Trimble, & C. Bennett (New York: American Institute of Physics), 297
Bertschinger, E., & Gelb, J. M. 1991, Computers in Physics, 5, 164
Blumenthal, G. R., Faber, S. M., Flores, R., & Primack, J. R. 1986, ApJ, 301, 27
Bond, J. R., Cole, S., Efstathiou, G., & Kaiser, N. 1991, ApJ, 379, 440
Brainerd, T. G., & Villumsen, J. V. 1992, ApJ, 394, 409
Broadhurst, T. J., Ellis, R. S., & Shanks, T. 1988, MNRAS, 235, 827
Carlberg, R. G., & Couchman, H. M. P. 1989, ApJ, 340, 47
Carlberg, R. G., Couchman, H. M. P., & Thomas, P. 1990, ApJ, 352, L29
Cen, R. Y., & Ostriker, J. P. 1992a, ApJ, 393, 22
———. 1992b, ApJ, 399, L113
Couchman, H. M. P. 1991, ApJ, 268, L23
Couchman, H. M. P., & Carlberg, R. G. 1992, ApJ, 389, 453
Cowie, L. L., Songaila, A., & Hu, E. M. 1991, Nature, 354, 460
Davis, M., Efstathiou, G., Frenk, C. S., & White, S. D. M. 1985, ApJ, 292, 371
Dekel, A., & Silk, J. 1986, ApJ, 303, 39
Dressler, A. 1979, ApJ, 231, 659
———. 1980, ApJ, 236, 351
———. 1991, ApJS, 75, 241
Dubinski, J., & Carlberg, R. G. 1991, ApJ, 378, 496
Efstathiou, G., Bernstein, G., Katz, N., & Guhathakurta, P. 1991, ApJ, 380, L47
Efstathiou, G., Bond, J. R., & White, S. D. M. 1992, MNRAS, 258, 1P
Efstathiou, G., Ellis, R. S., & Peterson, B. A. 1988a, MNRAS, 232, 431
Efstathiou, G., Frenk, C. S., White, S. D. M., & Davis, M. 1988b, MNRAS, 194, 503
Evrard, A. E., Summers, F. J., & Davis, M. 1994, ApJ, 422, 11
Faber, S. M., & Jackson, R. E. 1976, ApJ, 204, 668
Faber, S. M., Wegner, G., Burstein, D., Davies, R. L., Dressler, A., Lynden-Bell, D., & Terlevich, R. J. 1989, ApJS, 69, 763
Fabricant, D., & Gorenstein, P. 1983, ApJ, 267, 535
Felten, J. E. 1977, AJ, 82, 861
Franx, M., Illingworth, G., & Heckman, T. 1989, ApJ, 344, 613
Frenk, C. S., White, S. D. M., Davis, M., & Efstathiou, G. 1988, ApJ, 327, 507
Fukugita, M., Takahara, F., Yamashita, K., & Yoshii, Y. 1990, ApJ, 361, L1
Gelb, J. M. 1992, MIT Ph.D. thesis
Gelb, J. M., & Bertschinger, E. 1994, ApJ, 436, 000 (Paper II)
Guiderdoni, B., & Rocca-Volmerange, B. 1990, A&A, 227, 362
Gunn, J. E., & Gott, J. R. 1972, ApJ, 176, 1
Hockney, R. W., & Eastwood, J. W. 1982, Computer Simulation Using Particles (New York: McGraw-Hill)
Hoffman, Y., & Shaham, J. 1985, ApJ, 297, 16
Holtzman, J. A. 1989, ApJS, 71, 1
Katz, N., Hernquist, L., & Weinberg, D. H. 1992, ApJ, 399, L109
Katz, N., & White, S. D. M. 1993, ApJ, 412, 455
Kauffmann, G., & White, S. D. M. 1993, MNRAS, 261, 291
Kormendy, J. 1990, in Evolution of the Universe of Galaxies (ASP Conf. Ser., 10), 33
Kundić, T. 1991, S.B. thesis, MIT
Little, B., Weinberg, D. H., & Park, C. 1991, MNRAS, 253, 295
Melott, A. L. 1990, Phys. Rep., 193, 1
Mould, J. R., Oke, J. B., De Zeeuw, P. T., & Nemec, J. M. 1990, AJ, 99, 1823
Park, C. 1990, MNRAS, 242, 59
Pierce, M. J., & Tully, B. 1988, ApJ, 330, 579
Postman, M., & Geller, M. J. 1984, ApJ, 281, 95
Press, W. H., & Schechter, P. 1974, ApJ, 187, 425
Rubin, V. C., Burstein, D., Ford, W. K., & Thonnard, N. 1985, ApJ, 289, 81
Sargent, W. L. W., Young, P. J., Boksenberg, A., Shortridge, K., Lynds, C. R., & Hartwick, F. D. A. 1978, ApJ, 221, 731
Schechter, P. L. 1976, ApJ, 203, 297
Toth, G., & Ostriker, J. P. 1992, ApJ, 389, 5
Tsai, J. C. 1994, ApJ, 423, 143
Tully, R. B., & Fisher, J. R. 1977, A&A, 54, 661
Tully, R. B., & Fouque, P. 1985, ApJS, 58, 67
Tyson, J. A. 1988, AJ, 96, 1
Uson, J. M., Boughn, S. P., & Kuhn, J. R. 1991, ApJ, 369, 46
Warren, M. S., Zurek, W. H., Quinn, P. J., & Salmon, J. K. 1991, in After the First Three Minutes, ed. S. Holt, V. Trimble, & C. Bennett (New York: AIP), 216
White, S. D. M., Davis, M., Efstathiou, G., & Frenk, C. S. 1987, Nature, 330, 451
White, S. D. M., & Rees, M. 1978, MNRAS, 183, 341
White, S. D. M., & Sarazin, C. L. 1988, ApJ, 335, 688
Wright, E. L., et al. 1992, ApJ, 396, L13
Zel'dovich, Ya. B. 1970, A&A, 5, 84